

1 *In-situ* dynamic WetSEM imaging and electrical impedance  
2 measurements on Portland cement during early hydration  
3  
4  
5

6 Benny Suryanto\*, James O. Buckman, W. John McCarter, Hussameldin Taha  
7  
8  
9

10 School of Energy, Geoscience, Infrastructure and Society,  
11 Heriot-Watt University,  
12 Edinburgh, EH14 4AS,  
13 United Kingdom,  
14  
15  
16

17 \* Corresponding Author

18 E-mail: [b.suryanto@hw.ac.uk](mailto:b.suryanto@hw.ac.uk)

19 Tel: +44 (0)131 451 3817

20 Fax: +44 (0)131 451 4617  
21  
22

23 ORCID:

24 Benny Suryanto: 0000-0002-3979-9994

25 William J McCarter: 0000-0002-1949-2856  
26  
27

28 **Highlights**

- 29 • Dual testing methodology for *in-situ* monitoring of early hydration presented
- 30 • Automated image collection applied to the WetSEM technology for the first time
- 31 • WetSEM images correlate with data from electrical impedance measurements
- 32 • Portlandite precipitation alters both conduction and polarization processes
- 33 • Double-layer and interfacial processes give rise to the bulk polarization

34

35

36 **Abstract**

37 Wet scanning electron microscopy (WetSEM) and electrical impedance measurements have been  
38 employed to study the physico-chemical processes during the early hydration of Portland cement. The  
39 WetSEM study employed the Quantomix WetSEM capsule, allowing examination of the morphology  
40 of hydrating cement directly *in situ* via 36 semi-electron-transparent windows under SEM vacuum  
41 conditions over the initial 24-h after gauging whilst maintaining the test sample under atmospheric  
42 conditions. This qualitative assessment was used to aid interpretation of the stages of early hydration  
43 identified from impedance measurements, which were taken on a replicate specimen over the  
44 frequency range 1kHz–1MHz. It is shown that detailed frequency- and time- domain impedance  
45 measurements allowed identification of key processes during setting and early hardening which were  
46 correlated with data from the WetSEM study. Attention is directed to the sequence of hydration  
47 obtained from the two techniques and how they provide both supporting and complementary  
48 information.

49

50 **Keywords:** early hydration; electrical properties; cement; WetSEM; electrical impedance.

51

52

53

54

55 **1. INTRODUCTION**

56 Cement hydration is a dynamic process involving a series of complex and interrelated physico-  
57 chemical processes taking place immediately from gauging throughout setting and early hardening.  
58 Given that the early hydration of cement is exothermic by nature, these processes have been  
59 traditionally studied using isothermal conduction calorimetry and adiabatic temperature rise testing  
60 [1-6]. These methods do not, however, provide direct information on microstructural changes which  
61 are more relevant to long-term durability and performance of concrete. More advanced techniques  
62 have been employed in this respect, including environmental scanning electron microscopy (ESEM),  
63 transmission electron microscopy, nuclear magnetic resonance, ultrasonic pulse velocity, X-ray  
64 diffraction and X-ray tomography [see, for example, 7-15].

65

66 In terms of microstructural changes during early hydration, the present work employs the WetSEM  
67 technology [16] whereby a hydrating cement paste is continuously imaged under atmospheric  
68 conditions within an *environmental* capsule inside a scanning electron microscope (SEM) over a 24-h  
69 period after gauging. In traditional SEM operation, examination of cement hydration is generally  
70 made by stopping the hydration process at various stages, typically by plunging in liquid nitrogen or  
71 by high-pressure freezing before examination by cryo-SEM [17, 18]. Such studies are important as  
72 they address information on the physical changes of cement hydration over time. However, the action  
73 of freezing the hydration process, particularly plunge freezing, may introduce artefacts and not  
74 provide a true reflection of hydration processes in its natural state. To address this issue, the  
75 environmental SEM (ESEM) was developed to provide a high-resolution method of studying cement  
76 in its wet state [19-21]. However, artefacts can still be introduced during chamber pump-down and  
77 maintaining samples hydrated during hydration and curing, with associated exothermic reactions, has  
78 been proven to be difficult. This has led to the development of the WetSEM technology through the  
79 use of a WetSEM capsule (viz, the Quantomix [16, 22]). In essence, a WetSEM capsule offers a  
80 sealed micro-environment, impervious to vacuum, with access to the hydrating test sample through a  
81 series of semi-electron-transparent windows. As such, it is possible to minimize artefacts introduced

82 as a consequence of vacuum as in normal SEM operation. Such capsules are particularly useful for a  
83 range of materials, including biological specimens, pharmaceutical and hydraulic materials [16, 23-  
84 24].

85

86 *In-situ* dynamic imaging of cement hydration using WetSEM technology has now been demonstrated  
87 by several researchers. Katz et al. [16] was the first to employ this technology to follow the dynamic  
88 nature of the hydration process of gypsum and cement paste at varying water-to-binder ratios, with  
89 observations undertaken at magnifications up to 20k $\times$ . Whilst the study was carried out over a 24-h  
90 period, only interpretations at 6-h and 24-h of hydration were presented, with a highlight being made  
91 on the presence of Portlandite at 6-h and the development of calcium-silicate-hydrate (C-S-H) around  
92 cement grains, when observed at the end of the test period (24-h after gauging). The use of WetSEM  
93 at a prolonged exposure and higher magnifications than 10k $\times$  was not recommended as it can generate  
94 extra heat which may accelerate the hydration process. Gallucci and Scrivener [25] further discussed  
95 the strengths and limitations of the technology and highlighted the importance of sample preparation  
96 for successful imaging. In their study, repeated low-magnification observations were made to  
97 highlight the sequence of hydration during the early age and the precipitation of C-S-H was found not  
98 only around cement grains but also in the pore space between the grains. Hexagonal Portlandite was  
99 found to precipitate at less than 3 hours, which then eventually blocked the observation window at  
100 ~13-h, possibly due to prolonged beam heating. To minimize extra heat from the electron beam,  
101 Venkateela and Sun [26] employed the blank beam function in a SEM to facilitate repeated  
102 observations on a 15-min cycle during the initial eight hours after gauging. In their study, cement  
103 pastes with varying water-to-cement ratios were contained within WetSEM capsules and the images  
104 obtained from the repeated observations were then processed using image analysis. It was found that  
105 the water volume decreases with increasing hydration time while the total solid volume shows an  
106 opposite trend, which was interpreted as particle growth.

107

108 The primary aim of the present work is to employ two different, yet complimentary, experimental  
109 techniques:

- 110 (i) WetSEM, with the aim of providing qualitative information on the morphology of the  
111 hydration products during the initial stages of hydration; and,  
112 (ii) Electrical property and internal temperature measurements [27], with the aim of providing  
113 quantitative information on the physico-chemical processes occurring during early hydration.  
114

115 Regarding (i), an automated technique employing the WetSEM capsule is introduced for the first time  
116 to obtain time-lapse images of the physical and morphological changes within the paste throughout  
117 setting and early hardening. Regarding (ii), monitoring the electrical properties of cementitious  
118 systems represents a relatively simple testing technology to study setting and hardening under non  
119 iso-thermal conditions; samples are not necessarily restricted to cement pastes and mortars, concretes  
120 can also be studied [27, 28], thereby offering the potential for deployment in real-world concreting  
121 operations [29]. These two techniques differ in the information they provide and this paper attempts,  
122 for the first time, to correlate measurements obtained from WetSEM imaging with electrical  
123 impedance measurements.  
124

## 125 **2. EXPERIMENTAL PROGRAMME**

### 126 **2.1 Materials and sample preparation**

127 The cement paste was prepared using CEM I 52.5N to EN197-1 [30] (see the typical oxide  
128 composition in Table 1) and mains tap-water with a resistivity of  $\sim 160 \Omega\text{m}$ . These two materials were  
129 mixed at a relatively high water-to-cement ratio ( $w/c=0.55$ ) to ensure sufficient consistency for the  
130 WetSEM study, detailed below. All test samples were produced from the same bag of cement to  
131 minimize the influence of variability of materials on test results. The cement bag and the mixing water  
132 were pre-conditioned in a temperature controlled laboratory ( $22\pm 1^\circ\text{C}$ ) for more than 24-h prior to the  
133 start of testing.  
134

135 During the production of the sample for the WetSEM study detailed below, 0.5-litres of cement paste  
136 was hand mixed for 2-min and an aliquot was then pipetted into a Quantomix QX-102 capsule (see  
137 Fig. 1(a)). The capsule comprised two main parts: an upper cell into which the paste was injected and

138 a sealing stub which formed the base of the capsule. These two parts were connected by a flexible  
139 rubber packing to ensure air and water tightness, as well as relieving excessive pressure during cell  
140 closure. The upper cell had a semi-electron-transparent thin membrane, reinforced with metal grid to  
141 provide the required strength to withstand the pressure difference while under vacuum in the SEM.  
142 The metal grid divided the top membrane into 36 equally-sized semi-electron-transparent windows,  
143 resulting into an arrangement displayed in Fig. 1(b). In this figure, the white grid corresponds to the  
144 metal supporting frame whereas the black rounded squares represent the observation windows. It is  
145 through these windows that continuous imaging of the physical changes in the paste, which was in  
146 contact with, or in close proximity to, the inner surface of the membrane was possible, as it hydrated  
147 under atmospheric conditions.

148

149 Together with the sample for the WetSEM study, a paste specimen with the same w/c ratio was  
150 prepared for electrical measurements using a 2-litre Hobart planetary motion rotary mixer. The paste  
151 was mixed for 2-min before being compacted into a Plexiglas cuboidal cell with internal dimensions  
152  $50 \times 50 \times 50 \text{ mm}^3$  (see Figure 1(c)). Following a previous study [27], a pair of stainless steel pins (grade  
153 316L), each 2.4 mm in diameter, were embedded centrally inside the cell to a depth of 25 mm with a  
154 centre-to-centre spacing of 25 mm. Immediately after compaction, the top surface of the cell was  
155 covered with a plastic film to minimize evaporation and the cell was then contained within a benchtop  
156 climatic chamber at a temperature of  $22^\circ\text{C}$  and relative humidity of 95%.

157

## 158 **2.2 Measurements and data processing**

159 *Scanning electron microscope.* A Quanta 650 field-emission gun scanning electron microscope (FEI,  
160 Hillsboro, US) fitted with an Oxford Instruments X-max<sup>N</sup> 150 mm Energy Dispersive X-ray (EDX)  
161 detector was used for the study. Before starting the imaging sequence, one WetSEM capsule  
162 containing a freshly prepared paste was positioned onto the stage of the SEM, with the cell membrane  
163 facing the electron beam. Imaging was then taken using a backscattered electron (BSE) detector in  
164 high vacuum mode, with the SEM operating at 20 kV using a spot size of 5.2 and a working distance  
165 of 10mm [31].

166 Automated image acquisition was performed 10 minutes after gauging, using the FEI MAPS software  
167 (Version 2.1, 64-bit, FEI). The mapping process involved the acquisition of a series of BSE images  
168 across a regular tile pattern, following the sequence described in the schematic shown in Figure 1(d).  
169 From each individual tile, high resolution 4096×4096 (16M) pixels low magnification (600×) BSE  
170 image was acquired, starting from Tile 1 (top left) and then moving systematically from left-to-right  
171 and top-to-bottom toward Tile 36 (bottom right). At this resolution, it took approximately 35-min to  
172 obtain the image of the entire area (36 tiles). The same mapping process was then repeated until 24-h  
173 after gauging (or 42 times), producing a total of 1,512 images. The advantages of acquiring images in  
174 this manner are threefold:

- 175 (i) a reduction in the electron beam exposure which minimizes local heating and hence the  
176 risk of membrane failure due to electron beam heating;
- 177 (ii) minimize the additional heat generated by the electron beam thereby reducing its  
178 influence on the physico-chemical processes during the early hydration; and
- 179 (iii) generate 36 notionally identical samples from a single experiment run, allowing the  
180 evaluation of the inherent variability among the samples whilst maintaining the quality of  
181 individual images.

182 On completion of experiment, the individually acquired images were manually aligned using the  
183 GIMP software (Version 2.8.10) to form a time-lapse complete montage of the paste (see, for  
184 example, Fig. 2). The images were further processed to create GIF animations which are provided as a  
185 video component to the electronic version of this article.

186

187 *Electrical measurements.* An E4980AL high-precision LCR meter (Keysight, Santa Rosa, US) was  
188 used to perform a logarithmic impedance sweep at 61 spot frequencies within the range 1kHz-1MHz,  
189 under a signal amplitude of 350 mV. The LCR meter was controlled by a desktop PC using a custom-  
190 designed virtual instrument in LabVIEW (Version 2015, National Instruments, Austin, US).  
191 Communication with the LCR meter was established across a USB interface using Keysight IO  
192 Library Suite software (Version 2017.1). Electrical measurements were undertaken by connecting the  
193 electrodes to the voltage high/low and current output/input terminals in the LCR meter via

194 individually screened coaxial cables, with connection at the electrodes by means of alligator clips.  
195 Measurements were undertaken in voltage-drive mode on a four-minute cycle throughout the initial  
196 24-h after gauging. One measurement cycle over the full frequency range took approximately 15-s.  
197 The LCR meter was placed in standby mode between measurement cycles until the next measurement  
198 was triggered.

199

200 Lead inductive effects were *nulled* from the measured impedance response using a measurement  
201 correction protocol implemented in Microsoft Excel; full details of the protocol are provided  
202 elsewhere [32]. Two sets of calibration data were acquired prior to the start of experiment, comprising

- 203 (i) An open-circuit correction, with sweep measurement taken with the coaxial cables connected to  
204 the pin electrodes positioned within an empty cell; and  
205 (ii) A short-circuit correction, with sweep measurement taken on the same setup, but with the  
206 electrodes being short-circuited.

207 In addition to impedance measurements, the internal temperature of the test specimen and the climatic  
208 chamber were monitored every 2 minutes using a 5K thermistor via an auto-ranging data logger.

209

### 210 **2.3 Preliminaries for electrical measurements**

211 The electrical properties of a porous, saturated cementitious material rely on the ease with which  
212 charges can contribute to conduction and polarization processes within the system and depend,  
213 primarily, on the frequency of the applied electrical field and the time-variant nature of both the  
214 evolving pore structure and pore-fluid chemistry [33, 34]. To provide a detailed insight into chemical  
215 reactions, microstructural changes and pore structure development within a cement paste, these  
216 measurements are taken over three orders of magnitude of frequency (viz, 1kHz–1MHz).

217

218 From an electrical standpoint, the impedance,  $Z(\omega)$ , of a material at any angular frequency,  $\omega$ , can be  
219 written as,

220 
$$Z(\omega) = Z'(\omega) - iZ''(\omega) \quad (1)$$



221 where  $Z'(\omega)$  is the resistive (real) component (in Ohm),  $Z''(\omega)$  is the reactive (imaginary) component  
 222 (in Ohm),  $i = \sqrt{-1}$  and  $\omega = 2\pi f$  with  $f$  being the frequency of the applied field (Hz). At any  
 223 frequency, the electrical response of such a system will result from the superposed phenomena of  
 224 conduction and polarization which can be quantified, respectively, by the bulk conductivity,  $\sigma(\omega)$   
 225 (S/m), and the relative permittivity,  $\varepsilon_r(\omega)$ . These parameters can be de-embedded from the resistive  
 226 and reactive components by [35],

$$227 \quad \sigma(\omega) = \left( \frac{Z'(\omega)}{Z'(\omega)^2 + Z''(\omega)^2} \right) \frac{L}{A} \quad (2)$$

$$228 \quad \varepsilon_r(\omega) = \frac{1}{\varepsilon_0 \omega} \left( \frac{Z''(\omega)}{Z'(\omega)^2 + Z''(\omega)^2} \right) \frac{L}{A} \quad (3)$$

229 where  $\varepsilon_0$  is the permittivity of a vacuum ( $8.854 \times 10^{-12}$  Farads/m) and  $L/A$  (/m) is a factor which is  
 230 related to the electrode geometry and sample configuration. As the electrical field between the  
 231 electrodes is non-uniform, the geometrical constant  $L/A$  in above equations cannot be readily  
 232 calculated. This was thus determined by impedance measurements on a liquid of known conductivity  
 233 placed within the same test cell. For the electrode arrangements and test cell used in the current work,  
 234 the geometrical factor  $L/A$  was evaluated as  $34.92 \text{ m}^{-1}$ . Given that the relative permittivity calculated  
 235 using Eq. 3 can extend over several orders of magnitude, the term normalised permittivity, denoted  
 236  $\varepsilon_N(\omega)$ , is introduced to aid comparative analysis. This is defined as  $\varepsilon_{r,t}(\omega)/\varepsilon_{r,o}(\omega)$ , with  $\varepsilon_{r,o}(\omega)$   
 237 representing the measured permittivity at the start of the test and  $\varepsilon_{r,t}(\omega)$  representing the corresponding  
 238 value measured at time,  $t$ , after the start of the test.

239

### 240 **3. TEST RESULTS AND DISCUSSION**

#### 241 **3.1 *In-situ* dynamic imaging**

242 To provide a qualitative assessment of early hydration process, Figs. 2(a)–(d) present a complete  
 243 montage of the 36 individually acquired BSE images at four selected points in time during the 24-h  
 244 period. In the initial state displayed in Fig. 2(a), the bright dots correspond to the upper part of the  
 245 cement grains which was in close proximity or in contact with the inner surface of the semi-electron-  
 246 transparent membrane. The dots are surrounded by darker regions which occupy a larger fraction of

247 the observation windows and represent the interstitial aqueous phase between the cement grains. In  
248 some windows, the appearance of one to two large dark regions is evident, corresponding to the  
249 presence of occluded micro air voids which have adhered to the inner side of the membrane. Thin  
250 horizontal and vertical lines extending across the entire image are evident which indicate the grid/tile  
251 boundaries (see the gridlines in Fig. 1(d)). It is apparent from Figs. 2(a)–(d) that the vertical gridlines  
252 become progressively displaced to the right due to slight inherent drift in the electron beam. This does  
253 not, however, impair the usability of the proposed technique as the individually collected BSE images  
254 can be stitched together to construct the montage. Given the large area to scan and the considerable  
255 time required to follow the dynamic nature of the hydration process, it is essential to ensure that the  
256 electron beam source is stable, with regard to BSE intensity. This is required to remove inadvertent  
257 variance in BSE intensity which would render interpretation of the results difficult. The results  
258 presented in Figs. 2(a)–(d) reveal that this is not an issue as all windows within each figure display  
259 comparable brightness with no notable variations in BSE intensity levels.

260

261 With reference to Figs. 2(a)–(d), it is evident that as hydration reactions progress, the water level  
262 within the capsule subsides with time revealing a porous surface comprising partially hydrated cement  
263 grains which are bright and pore space which is dark (see Figs. 2(c) and (d)). At the same time, the  
264 interstitial pore space is also progressively filled by hydration products although most of this space is  
265 covered by water which is not electron transparent and hence most of this infilling process remains  
266 undetectable. Another prominent feature from Figs. 2(c) and (d) relates to the presence of large,  
267 elongated, bright crystals of Portlandite which are scattered over the top surface of the paste. The  
268 amount and geometry of this crystal formation varies from one window to another and would be  
269 indicative of inherent variability in the available pore space between the cement grains and in the  
270 concentration of  $\text{Ca}^{2+}$  in the interstitial aqueous phase.

271

272 To provide a better insight into the process of cement hydration, the complete time-lapse BSE images  
273 for Window 14 (3-6 in Fig. 1(b)) are displayed in Fig. 3. This is also provided as a video component  
274 to the electronic version of this article; to access this video component, simply click on the image

275 visible below (see Video 1 in the electronic version of this article). As before, the upper part of the  
276 cement particles which was in close proximity or in contact with the membrane was observed as  
277 bright dots, whereas the liquid covering the remainder of the particles is shown as dark areas. No  
278 obvious differences in morphology are evident during the initial state i.e. the first three images,  
279 indicating that there have been no significant physical changes to the cement grains when observed at  
280 this low magnification. The first prominent feature can be seen from ~1-h 45-min after gauging, or  
281 image 4 on Fig. 3 where the precipitation of elongated, calcium-rich crystals (i.e. Portlandite) are  
282 evident in the water-filled capillary space between the grains, as indicated by the circle in image 4  
283 (Fig. 3). The nucleation of Portlandite at this early age agrees with the findings of Gallucci and  
284 Scrivener [25] although in their study this was observed at a later stage (~3-h after gauging). Marked  
285 crystal growth is evident from the successive images displayed in Fig. 3, transforming into a *massive*  
286 crystal which is angular in shape with smooth sides and some perforations. To highlight the growth  
287 process, enlarged images of the area indicated by the rectangles in images 8, 14, 21 and 32 in Fig. 3  
288 are presented in Figs. 4(a)–(d); for clarity, the lime-lapse images of this crystal growth are also  
289 included as Video 2 in the electronic version of this article. The nucleation of similar crystals but  
290 varying in size and shape is evident in Fig. 3 throughout the 24-h test period. Apart from Portlandite,  
291 the precipitation of much smaller hydration products is also apparent on the grain surface (see, for  
292 instance, Fig. 4(d)) and is discussed below. It is also evident from Fig. 3 that the exposed surface of  
293 the cement grains (the bright dots) becomes brighter and the free water-content of the paste reduces  
294 with time, which is indicative of water consumption resulting from the hydration reactions and could  
295 give a false impression of particle growth viz. the gradual decrease in water-level is interpreted  
296 exclusively as particle growth.

297

298 Another notable feature from Fig. 3 (and Video 1) is related to the increasing rate of reduction in free  
299 water-content resulting from the hydration reactions from ~8-h (image 14), thereby exposing the  
300 underlying structures comprising partially hydrated cement particles and capillary pores (dark  
301 regions). This is highlighted on the image by the two circled areas, with the enlarged version  
302 displayed in Figs. 4(e) and (f). As hydration progresses, the free water-content continues to reduce,

303 most notably from ~10-h after gauging (see image 18 onwards on Fig. 3), signifying a period of  
304 chemical activity. The result is a porous surface which has been depleted of water, giving a *coral reef*  
305 appearance.

306

307 Fig. 5 displays BSE images of Window 2 (1-4 on Fig. 1(b)) at six selected times over the 24-h test  
308 period, with four enlarged images at 24-hours presented in Figs. 6(a)–(d) and the corresponding video  
309 component included as Video 3 in the electronic version of this article. It is evident from Fig. 5 that  
310 the sequence of events is comparable to those presented earlier in Fig. 3, although the time that  
311 corresponds to a particular event varies to some extent from one window to another indicating the  
312 temporal and spatial variations in hydration response. This includes: (i) the time at which the  
313 Portlandite starts to crystalize; and (ii) the time when the interstitial aqueous phase starts decrease.  
314 Fig. 8, for clarity, presents the respective times for each window at which Portlandite appears and the  
315 decreasing free water-content process starts; the mean values were found to be, respectively, 2-h 15-  
316 min with a coefficient of variation (CoV) of 33% and 8-h 25-min with a CoV of 20%.

317

318 With reference to the enlarged images taken at 24-h, it is evident from Figs. 6(a)–(d) that the large  
319 Portlandite crystals are surrounded by cement grains covered by fibrillar outgrowths comprising C-S-  
320 H and some longer, needle-like (ettringite) crystals [15, 17, 21, 36, 37]. To highlight the growth  
321 process of these crystals, Figs. 7(a)–(f) present the time-lapse of Fig. 6(d) at 2.5-h, 4-h, 6.5-h, 8-h, 10-  
322 h and 12.5-h after gauging, with the complete time-lapse provided as Video 4 in the electronic version  
323 of this article. No notable outgrowth from the grain surface are apparent at 2-h (Fig. 7(a)), although  
324 local precipitation may have occurred on the grain surface (see, for instance, [17]). However, this  
325 remains undetected as it is beyond the resolution of the acquired BSE image. Notable outgrowths are  
326 evident from ~4-h after gauging (Fig. 7(b)), with a more rapid outgrowth detected from ~6.5-h after  
327 gauging (Fig. 7(c)), which continued over the remainder of the test period (viz, Figs. 6(d) and 7(d)–  
328 (f)). To obtain more detailed insights into the hydration processes on the grain surface, further  
329 research involving the freezing of cement paste sample at various stages of hydration and further  
330 examination by cryo-SEM is required.

331 Figs. 9(a) and (b) present, respectively, the BSE images and elemental EDX maps of Windows 11, 12,  
332 17, 18, 24 and 25 (see Fig. 1(d)) at 24-h after gauging. Figs. 9(c) and (d) present an enlargement of the  
333 selected area shown in Window 18 (on Fig. 9(a)) and the respective elemental EDX map whose  
334 spectra are presented in Fig. 9(e). The map indicates that the large bright crystal displayed in the BSE  
335 image in Fig. 9(c) is calcium rich which agrees with the strong peak of calcium in Spectrum 1 (Fig.  
336 9(e)), indicating Portlandite. Spectrum 2, representing the darker area in Fig. 9(c), displays strong  
337 peaks due to calcium and silicon from calcium-silicate-hydrate (C-S-H) [38] (similar to the  
338 precipitates covering the cement grains presented earlier in Figs. 6(c)), and weak peaks due to  
339 aluminium and sulphur from monosulphoaluminate (AFm) and ettringite (AFt) [38]. While hydrogen  
340 is a key component in C-S-H, it does not appear in the elemental analysis as it has only one electron-  
341 shell, and hence is not X-ray reflective. Spectrum 3 displays strong peaks due to silicon from the  
342 silicate phase in the cement and other peaks due to calcium, aluminium, potassium and sulphur.  
343 Spectra 4, 5 and 6 display strong peaks due to calcium, aluminium and silicon and weak peaks due to  
344 magnesium, sulphur, potassium and iron, suggesting the presence of partially hydrated aluminate and  
345 ferrite crystals covered by hydrates comprising C-S-H and ettringite (AFt) [38, 39].

346

## 347 **3.2 Electrical property measurement**

### 348 *3.2.1 Preliminaries*

349 Immediately on gauging, cement and water takes the form of a heterogeneous colloidal suspension  
350 which gradually turns into a solid matrix through a series of complex physico-chemical processes.  
351 Under the action of an alternating electrical field, some charges (ions in solution) are free to drift  
352 through the continuous aqueous phase and discharge at the electrodes, producing an ionic conduction  
353 effect. Other charges, which are electrostatically held onto grain or gel surfaces, oscillate about their  
354 zero-field equilibrium position in sympathy with the alternations of the electric field. This can induce  
355 large dipole moments which increases the overall polarizability of the system (see Fig. 10(a)). This is  
356 a low-frequency polarization mechanism and generally referred to as the double-layer polarization  
357 [40, 41]. In addition to this mechanism, albeit operating over an intermediate frequency (high kHz–  
358 MHz), is an interfacial polarization process [42] which is schematically shown in Fig. 10(b). As

359 hydration progresses, free charges in the aqueous phase may accumulate at internal interfaces within  
360 the material; whilst such charges do not contribute to the overall ionic conduction process, it increases  
361 the polarizability of the paste. The polarizability of the system can be quantified by the relative  
362 permittivity (Eq. 3) whereas the conductive effect can be quantified by the bulk conductivity (viz, Eq.  
363 2). Given that both parameters are influenced by free and bound charges, the measurement of both  
364 parameters throughout setting and hardening processes could offer detailed insights into the dynamic,  
365 time-variant nature of early hydration.

366

### 367 3.2.2 Interpretation of test results

368 To provide a quantitative assessment of the physical changes and chemical processes during the early  
369 hydration process, the electrical response of the cement paste is discussed below. For clarity, only  
370 every 10<sup>th</sup> data marker is highlighted on Figs. 11(a)–(c).

371

372 Fig. 11(a) presents the change in the conductivity,  $\sigma(\omega)$ , over the 24-hour test period together with its  
373 derivative,  $d\sigma/dt$ , with the conductivity presented at a frequency of 100kHz. This frequency was  
374 found high enough to ensure that the influence of electrode polarization was negligible (discussed  
375 below), thereby allowing accurate evaluation of the bulk response. The change in normalised relative  
376 permittivity,  $\epsilon_N(\omega)$ , during the same test period is presented in Fig. 11(b). While data were measured  
377 at 20 frequencies per decade over the frequency range 1kHz–1MHz,  $\epsilon_N(\omega)$  is only presented at five  
378 spot frequencies viz. 1kHz, 100kHz, 250kHz, 500kHz and 1MHz, with  $\epsilon_{r,o}(\omega)$  presented in Table 2. In  
379 general terms, the conductivity increases up to ~1-h 40-min and then decreases over the remainder of  
380 the test period, with a weakly developed *shoulder* detected between 8-h and 12-h.  $\epsilon_N(\omega)$  measured at  
381 1kHz, 100kHz and 250kHz (Fig. 11(b)) displays a similar trend to the conductivity, with the shoulder  
382 becoming more prominent with increasing frequency of applied field. The shoulder is, however,  
383 absent at higher frequencies (viz, 500 kHz and 1 MHz) and  $\epsilon_N(\omega)$  displays a monotonic increase from  
384 ~8-h.

385

386 On closer examination, the conductivity response and its derivative,  $d\sigma/dt$ , can be further subdivided  
387 into six distinct regions indicated I–VI in Figs. 11(a)-(c) to highlight several stages of the hydration  
388 process. This was possible due to the short time interval between sweep measurements, allowing more  
389 detailed information than was previously available over the frequency range under consideration.  
390 Note that reference to the WetSEM images below mainly relates to Fig. 3 (and Video 1 in the  
391 electronic version of this article).

392

393 ***Region I: 0 – 20-min (WetSEM Images 1 and 2)***

394 This region is characterised by a rapid increase in conductivity and a positive rate of change of  
395 conductivity (i.e.  $d\sigma/dt$ ), with  $d\sigma/dt$  decreasing with time. The increase in conductivity is attributed to  
396 the rapid dissolution of alkalis and sulphate ( $\text{Na}^+$ ,  $\text{K}^+$ ,  $\text{Ca}^{2+}$ ,  $\text{SO}_4^{2-}$  and  $\text{OH}^-$ ) into the aqueous phase and  
397 is accompanied by an increase in internal temperature as shown in Fig. 11(c). The reduction in  $d\sigma/dt$   
398 over this period would indicate that the surfaces of the cement grains are gradually covered by early  
399 hydration products thereby hindering the dissolution process, and hence an overall reduction in  
400 reaction rate. These physical changes were, however, not detectable in WetSEM study as such  
401 changes occur locally on the grain surface which was masked by the gauging water which is not  
402 electron transparent.

403

404 The rapid increase in  $\epsilon_N(\omega)$  (Fig. 11(b)) occurring concurrently at all selected frequencies mimics the  
405 rise in conductivity and would imply an increasing amount of charges developing on the grain  
406 surface, forming an electrical double layer (see Fig. 10(a)). Polarization of the double-layer can  
407 induce high permittivity values [40-42]; however, superimposed upon this polarization mechanism  
408 will be electrode polarization effects [43-45]. Electrode polarization is a low-frequency process which  
409 reduces with increasing frequency of applied field. At 1kHz, electrode effects will make a substantial  
410 contribution to the permittivity and it is only at higher frequencies ( $\geq 100\text{kHz}$ ) that the true bulk  
411 response will be revealed over this Region. Confirmation of this comes from the fact that  $\epsilon_{r,o}(\omega)$  (see  
412 Table 2) decreases by more than three orders of magnitude as the frequency increases by two decades

413 from 1kHz ( $\epsilon_{r,o} = 7.49 \times 10^6$ ) to 100kHz ( $\epsilon_{r,o} = 2.11 \times 10^3$ ) whereas  $\epsilon_{r,o}(\omega)$  changes by approximately one  
414 order of magnitude as the frequency increases by two decades from 100kHz to 1MHz ( $\epsilon_{r,o} = 1.42 \times 10^2$   
415 at 1MHz). As the test frequency increases from 100kHz to 1MHz, it becomes more difficult for ions  
416 in the diffuse double-layer to follow the alternations of the electrical field which results in a reduction  
417 in permittivity with increasing frequency as presented in Table 2.

418

419 ***Region II: 20-min – 1-h 40-min (WetSEM Images 2 thru 4)***

420 This region is characterised by a slower increase in conductivity and a reducing value of  $d\sigma/dt$  (Fig.  
421 11(a)). This implies that the dissolution process continues albeit at a reduced rate, possibly due to  
422 early hydrate formation around the cement grains such as ettringite and C-S-H [17, 36, 37]. Over this  
423 period, the internal temperature of the cement paste reduces, approaching the ambient temperature  
424 (Fig. 11(c)). Despite the initial growth on the cement grains, the  $\epsilon_N$  response presented in Fig. 11(b)  
425 displays a similar trend to that of the conductivity implying that, at this w/c ratio, double-layer  
426 processes dominate over any reduction in charge mobility due to initial hydrate formation.  
427 Unfortunately, these physical changes are not evident under the WetSEM as they were masked by the  
428 gauging water. The conductivity and relative permittivity at all selected test frequencies reach their  
429 maximum values at the end of this Region.

430

431 ***Region III: 1-h 40-min – 2-h 10-min (WetSEM Images 4 and 5)***

432 This is a short-lived region and marks a sudden reduction in conductivity, indicated by the change  
433 from a period of increasing conductivity to a period of decreasing conductivity over the remainder of  
434 the 24-h period. The decrease in conductivity within this region is very rapid as  $d\sigma/dt$  reaches its  
435 global minimum (see Fig. 11(a)). It is now proposed that the sudden reduction in conductivity is  
436 associated with the crystallization of Portlandite infilling the water-filled capillary space between the  
437 grains as the time of occurrence of this Region coincides with the time of occurrence of Portlandite  
438 formation observed in the WetSEM study at 2-h 15-min (see Fig. 8). The slight difference in time is  
439 attributed to the fact that whilst the precipitation of Portlandite occurs within the entire volume of the



440 paste, only precipitates which are in contact with, or in close proximity to, the inner surface of the  
441 semi-electron-transparent membrane are detectable in the WetSEM and hence the apparent delay of  
442 its occurrence. Portlandite formation between the cement grains will limit the concentration of  $\text{Ca}^{2+}$  in  
443 the aqueous phase (or even result in a concentration reduction when the gypsum is depleted [46-47])  
444 and in more discontinuous and tortuous electrolytic conduction pathways, both of which would have  
445 the effect of decreasing the overall conductivity. Video 2 in the electronic version of this article  
446 displays the time-lapse of Portlandite growth observed in Window 14 throughout the test period.

447

448 Occurring in parallel with the decrease in conductivity in Fig. 11(a) is a corresponding reduction in  $\epsilon_N$   
449 (see Fig. 11(b)). The reduction in polarizability of the paste (hence  $\epsilon_r$ ) is now attributed to the  
450 formation of Portlandite crystals within the microstructure which will reduce charge concentration  
451 and mobility. Despite the formation of Portlandite, the internal temperature of the paste over this  
452 Region continues to decrease, as shown in Fig. 11(c).

453

#### 454 ***Region IV: 2-h 10-min – 8-h (WetSEM Images 5 thru 14)***

455 From Fig. 11(a), the conductivity over this period continues to decrease whereas  $d\sigma/dt$  remains  
456 relatively constant up to ~4-h, thereafter decreasing over the remainder of this Region. The decrease  
457 in  $d\sigma/dt$  at ~4-h coincides with the increase in internal temperature at this time (Fig. 11(c)) which  
458 would indicate the start of a period of chemical activity. It is proposed that this feature is due to  
459 secondary reactions on the  $\text{C}_3\text{S}$  phase and the gradual formation of a more crystalline microstructure.  
460 The continual decrease in conductivity could be attributed to the continuous growth of Portlandite  
461 (see Figs. 3, 4(a) and (b), and Video 2) and C-S-H crystals (see Figs. 6(d), 7(a)-(f) and Video 4),  
462 causing an increase in rigidity of the paste.

463

464 In a similar fashion, Fig. 11(b) shows that the permittivity of the paste continues to decrease over this  
465 Region, although this decrease becomes less pronounced with increasing frequency. Indeed, over the  
466 period 4-h to 8-h, the permittivity at 500kHz and 1MHz starts to display a slight increase. At these

467 higher frequencies, it is expected that the increase in permittivity must involve a short-range  
468 movement of charges occurring locally on grain surfaces or at crystal boundary interfaces (see, for  
469 instance, Figs. 7(a)-(d) or Video 4). Regarding the latter, the increasing surface area of the cement  
470 grains due to the formation and outgrowth of ettringite and C-S-H crystals would increase the  
471 polarizability of the paste through enhanced double-layer and interfacial processes.

472

473 ***Region V: 8-h – 12.5-h (WetSEM Images 14 thru 22)***

474 The conductivity continues to decrease although a *shoulder* occurs in the response which results in a  
475 local maximum on the  $d\sigma/dt$  curve over the central portion of this Region and a local minimum at the  
476 end. Interestingly, at 100kHz and 250kHz, the permittivity also displays a local maximum, whereas at  
477 500kHz and 1MHz the permittivity shows a continual increase over this Region. The conduction and  
478 polarization processes within the paste can result from several synergistic effects:

- 479 (i) the continuous growth of Portlandite and a more rapid outgrowth of fibrillar C-S-H crystals  
480 from the grain (see Figs. 7(e) and (f) or Video 4), resulting in an increase in surface area hence  
481 enhanced double-layer polarization on crystal surfaces. Conduction, on the other hand, would  
482 be reduced due to the development of more tortuous continuous pathways;
- 483 (ii) a release of ions into the capillary pore network through renewed chemical activity such as the  
484 transformation of AFt to AFm, with the subsequent release of  $Ca^{2+}$  and  $SO_4^{2-}$ , and reaction on  
485 the  $C_3A$  phases releasing alkalis bound up in them. This would increase conductive processes  
486 and enhance the polarizability of the paste through both interfacial and double-layer effects;
- 487 (iii) the accretion and infilling of the pore space by the products of hydration thereby forming a  
488 rigid structure which would serve to decrease both the conduction and polarizability of the  
489 paste due to space restriction and reduced charge mobility; and,
- 490 (iv) as the paste is hydrating under non-isothermal conditions, the increase in temperature would  
491 result in an increase in charge mobility, thereby increasing both polarization and conductive  
492 processes [48]. However, as the temperature rise within the paste is  $<1^\circ C$  over this Region, this  
493 effect is considered negligible in comparison to the influence of (i)-(iii) above.

494

495 From the WetSEM study presented in Fig. 3 (images 14–22) and Video 1, it is evident that the intense  
496 chemical activity also has the effect of increasing water consumption thereby causing a reduction in  
497 the free water-content. This is estimated as occurring at ~8-h 25-min (see Fig. 8) and coincides with  
498 the beginning of Region V. It is interesting to note from images 14–22 in Fig. 3 and Figs. 4(b) and (c)  
499 that the growth of Portlandite over this Region did not displace the surrounding cement particles  
500 which were much smaller in size, indicating that the hydration products at this stage were sufficiently  
501 strong to hold the particulate material within the aqueous paste together. At the end of this region, the  
502 products of hydration (Portlandite and gel) have resulted in a percolated pore network thereby  
503 forming a rigid matrix.

504

505 ***Region VI: 12.5-h – end of test (WetSEM Images 22 thru 42)***

506 This final region identified within the 24-h test period is characterized by a continual decrease in  
507 conductivity due to continued crystal growth and microstructural densification, resulting in a more  
508 tortuous, constricted and disconnected capillary pore network (see Videos 1–4). The  $\epsilon_N$  response at  
509 100kHz and 250kHz is similar to the conductivity as it displays a decreasing trend; however, at  
510 500kHz and 1MHz, the permittivity increases with time. Regarding the increase in polarizability of  
511 the paste at 500kHz and 1MHz, this could result from increased interfacial processes at crystal  
512 boundary interfaces within the pore structure (see Fig. 10(b)), resulting from an increase in ionic  
513 concentrations in the pore fluid i.e. the continued release of ions from the AFt to AFm transformation.  
514 Interfacial polarization is a high frequency process and is only revealed – i.e. becomes more dominant  
515 over double-layer effects – as the frequency increases. As there is no detectable increase in  
516 conductivity caused by release of ions into the pore network, it would indicate that changes in the  
517 pore structure due to hydration are having a dominant influence on the conductivity of the paste than  
518 changes in pore-fluid chemistry.

519

520

#### 521 4. Conclusions and Concluding Comments

522 Dual testing methodology utilizing electrical impedance measurements and WetSEM observations  
523 have been presented to provide information of the stages in the early hydration and complementary  
524 information on hydrate formation and crystal morphology. With regard to the impedance  
525 measurements, these were presented as conductivity ( $\sigma$ ) and permittivity ( $\epsilon_r$ ), with the permittivity  
526 presented over the frequency range 1kHz–1MHz. The WetSEM observations were undertaken on a  
527 sealed vacuum-tight miniature capsule via 36, 300- $\mu$ m square semi-electron-transparent windows and  
528 a novel, fully automated image collection technique was used to allow *in-situ* dynamic imaging under  
529 atmospheric conditions. The following conclusions can be drawn from this study:

- 530 1. The conductivity ( $\sigma$ ), its rate of change  $d\sigma/dt$  and the relative permittivity ( $\epsilon_r$ ) could be  
531 divided into six distinct regions which were used to identify key stages in the early hydration  
532 of cement paste. Over the frequency range 1kHz-1MHz, unlike the conductivity, the  
533 permittivity response changed markedly with electrode polarization processes dominant at  
534 low frequencies; however, at frequencies  $>100$ kHz the bulk response was revealed and related  
535 to double-layer and interfacial polarization processes occurring within the paste.
- 536 2. The WetSEM study revealed the nucleation of large, angular Portlandite crystals between the  
537 cement grains from ~2-h 15-min after gauging. This feature was coincident with the  
538 significant decrease in both conductivity and relative permittivity which took place at this  
539 time (*viz*, Region III).
- 540 3. The first half of Region IV is characterised by a reduction in conductivity and an almost  
541 constant  $d\sigma/dt$  value. The decrease in conductivity could be associated with the continuous  
542 growth of Portlandite, as observed in the WetSEM study over the same period. This was then  
543 followed by a reduction in  $d\sigma/dt$  (*viz*, become more negative) and an increase in internal  
544 temperature, indicating the start of a period of renewed chemical activity. During this period,  
545 a slight increase in permittivity at high frequencies (*viz*, 500kHz and 1MHz) was observed,  
546 occurring concurrently with the outgrowth of ettringite and C-S-H crystals from the WetSEM  
547 study. The increase in permittivity was as a result of the increase in the surface area of the

548 cement grains which increased the polarizability of the paste through enhanced double-layer  
549 and interfacial polarization processes.

550 4. The WetSEM study detected a reduction in the water-content of the paste at ~8-h 25-min after  
551 gauging which was coincident with the beginning of Region V identified from conductivity  
552 and relative permittivity measurements. The electrical measurements also underwent  
553 significant changes over Region V and explained in terms of dissolution processes and  
554 hydrate formation on grain surfaces.

555 5. Region VI is characterized by a continual decrease in internal temperature, conductivity and  
556  $d\sigma/dt$  due to continued crystal growth and microstructural densification, as observed in the  
557 WetSEM study.

558

#### 559 **Acknowledgements**

560 The authors gratefully acknowledge the support of the School of Energy, Geoscience, Infrastructure  
561 and Society for placing the facilities of the School at their disposal. Datasets from this study are  
562 available upon request from the lead author (b.suryanto@hw.ac.uk).

563

#### 564 **References**

565 [1] D.D. Double, A. Hellowell, S.J. Perry, The hydration of Portland cement, Proc. R. Soc. Lond. A.,  
566 Vol. 359, Mar. 1978, pp. 435–451.

567 [2] K.A. Paine, L. Zheng, R.K. Dhir, Experimental study and modelling of heat evolution of blended  
568 cements, Adv. Cem. Res. 17 (3) (2005) 121–132.

569 [3] L. Wadsö, M. Arndt, An international round robin test on isothermal (conduction) calorimetry for  
570 measurement of three-day heat of hydration of cement, Cem. Concr. Res. 79 (2016) 316–322.

571 [4] A. Arora, G. Sant, N. Neithalath, Ternary blends containing slag and interground/blended  
572 limestone: Hydration, strength, and pore structure, Const. Build. Mater. 102 (1) (2016) 113–124.

573 [5] T. Kishi, K. Maekawa, Multi-component model for hydration heating of Portland cement, Concr.  
574 Lib. JSCE 28 (1) (1996) 97–115.

575 [6] G.H. An, J.M. Park, S.L. Cha, J.K. Kim, Development of a portable device and compensation  
576 method for the prediction of the adiabatic temperature rise of concrete, *Constr. Build. Mater.* 102 (1)  
577 (2016) 640–647.

578 [7] D.A. Lange, K. Sujata, H.M. Jennings, Observations of wet cement using electron microscopy,  
579 *Ultramicroscopy* 37 (1–4) (1991) 234–238.

580 [8] K.L. Scrivener, Microscopy methods in cement and concrete science, *World Cem.* 28 (9) (1997)  
581 121–126.

582 [9] D. Gastaldi, F. Canonico, L. Capelli, E. Boccaleri, M. Milanesio, L. Palin, G. Croce, F. Marone,  
583 K. Mader, M. Stampanoni, In situ tomographic investigation on the early hydration behaviors of  
584 cementing systems, *Constr. Build. Mater.* 29 (2012) 284–290.

585 [10] Z. Liu, Y. Zhang, G. Sun, Q. Jiang, Observation of microstructure formation process of cement  
586 paste using non-destructive methods, *Mag. Concr. Res.* 64 (11) (2012) 957–965.

587 [11] C. Hu, Y. Han, Y. Gao, Y. Zhang, Z. Li, Property investigation of calcium–silicate–hydrate (C–  
588 S–H) gel in cementitious composites, *Mater. Charact.* 95 (2014) 129–139.

589 [12] C.A. da Luz, R.D. Hooton, Influence of curing temperature on the process of hydration of  
590 supersulfated cements at early age, *Cem. Concr. Res.* 77 (2015) 69–75.

591 [13] M. Moradian, H. Qinang, M. Aboustait, M.T. Ley, J.C. Hanan, X. Xiao, G.W. Scherer, Z. Zhang,  
592 Direct observation of void evolution during cement hydration, *Mater. Des.* 136 (2017) 137–149.

593 [14] O. Wenzel, M. Schwotzer, E. Müller, V.S.K. Chakravadhanula, T. Scherer, A. Gerdes,  
594 Investigating the pore structure of the calcium silicate hydrate phase, *Mater. Charact.* 133 (2017) 133–  
595 137.

596 [15] Z. Zhang, G.W. Scherer, A. Bauer, Morphology of cementitious material during early hydration,  
597 *Cem. Concr. Res.* 107 (2018) 85–100.

598 [16] A. Katz, A. Bentur, K. Kovler, A novel system for in-situ observations of early hydration  
599 reactions in wet conditions in conventional SEM, *Cem. Concr. Res.* 37 (1) (2007) 32–37.

600 [17] M. Fylak, J. Goske, W. Kachler, R. Wenda, H. Pollmann, Cryotransfer scanning electron  
601 microscopy for the study of cementitious systems, *Microscopy Anal.* 114 (2006) 9–12.

602 [18] A. Zingg, L. Holzer, A. Kaech, F. Winnefeld, J. Pakusch, S. Becker, L. Gauckler, The  
603 microstructure of dispersed and non-dispersed fresh cement pastes—new insight by cryo-microscopy,  
604 *Cem. Concr. Res.* 38 (4) (2008) 522–529.

605 [19] C.S. Deng, C. Breen, J. Yarwood, S. Habesch, J. Phipps, B. Craster, G. Maitland, Ageing of  
606 oilfield cement at high humidity: a combined FEG-ESEM and Raman microscopic investigation, *J.*  
607 *Mater. Chem.* 12 (10) (2002) 3105–3112.

608 [20] G. Ye, J. Hu, K. van Breugel, P. Stroeven, Characterization of the development of microstructure  
609 and porosity of cement-based materials by numerical simulation and ESEM image analysis, *Mater.*  
610 *Struct.* 35 (10) (2002) 603–613.

611 [21] Y. Sakalli, R. Trettin, Investigation of C3S hydration by environmental scanning electron  
612 microscope, *J. Microscopy* 259 (1) (2015), 53–58.

613 [22] S. Atkinson, Novel membrane-related technologies aid biological analyses, *Membr. Tech.* 5  
614 (2004) 5–7.

615 [23] S. Thiberge, A. Nechushtan, D. Sprinzak, O. Gileadi, V. Behar, O. Zik, Y. Chowers, S. Michaeli,  
616 J. Schlessinger, E. Moses, Scanning electron microscopy of cells and tissues under fully hydrated  
617 conditions, *Proc. Natl. Acad. Sci. USA*, Vol. 101, No. 10, 2004, pp. 3346–3351.

618 [24] J.C. Molero, S. Lee, I. Leizerman, A. Chajut, A. Cooper, K. Walder, Effects of rosiglitazone on  
619 intramyocellular lipid accumulation in *Psammomys obesus*, *BBA-Mol. Basis Dis.* 1802 (2) (2010)  
620 235–239.

621 [25] E. Gallucci, K. Scrivener, In situ dynamic SEM imaging of hydration of cement using WETSEM  
622 technology, *Adv. Appl. Ceram.* 106 (6) (2007) 319–326.

623 [26] G. Venkateela, Z. Sun, In situ observation of cement particle growth during setting, *Cem. Concr.*  
624 *Compos.* 32 (3) (2010) 211–218.

625 [27] H.M. Taha, W.J. McCarter, B. Suryanto, G. Starrs, Frequency- and time-domain dependency of  
626 electrical properties of cement-based materials during early hydration, *ASTM Adv. Civ. Eng. Mat.* 6  
627 (2) (2017) 65–83.

628 [28] B. Suryanto, W.J. McCarter, G. Starrs, T.M. Chrisp, Characterization of fly-ash using  
629 electrochemical impedance spectroscopy, *Procedia Eng.* 171 (2017) 705–714.

630 [29] W.J. McCarter, T.M. Chrisp, G. Starrs, A. Adamson, E. Owens, P.A.M Basheer, S.V.  
631 Nanukuttan, S. Srinivasan, N. Holmes, Developments in performance monitoring of concrete exposed  
632 to extreme environments, *ASCE J. Infra. Sys.* 18 (3) (2011) 167–175.

633 [30] British Standards Institution (BSI), EN197-1:2000, Cement-Part 1: Composition, specifications  
634 and conformity criteria for common cements, BSI, London, 2000.

635 [31] B. Suryanto, J.O. Buckman, P. Thompson, M. Bolbol, W.J. McCarter, Monitoring micro-crack  
636 healing in an engineered cementitious composite using the environmental scanning electron  
637 microscope, *Mater. Charact.* 119 (2016) 175–185.

638 [32] B.J. Christensen, R.T. Coverdale, R.A. Olson, S.J. Ford, E.J. Garboczi, H.M. Jennings, T.O.  
639 Mason, Impedance spectroscopy of hydrating cement-based materials: measurement, interpretation,  
640 and application, *J. Am. Ceram. Soc.* 77 (11) (1994) 2789–2804.

641 [33] W.J. McCarter, The a.c. impedance response of concrete during early hydration, *J. Mater. Sci.* 31  
642 (1996) 6285–6292.

643 [34] W.J. McCarter, G. Starrs, T.M. Chrisp, Electrical monitoring methods in cement science, in: P.  
644 Barnes and J. Bensted (Eds.), *Structure and Performance of Cements*, Second Edition, Spon Press,  
645 London 2002, pp. 442–456 (ISBN 0-203-47778-2).

646 [35] B. Suryanto, W.J. McCarter, G. Starrs, G.V. Ludford-Jones, Electrochemical immittance  
647 spectroscopy applied to a hybrid PVA/steel fiber engineered cementitious composite, *Mater. Des.* 105  
648 (2016) 179–189.

649 [36] R. Ylmén, U. Ulf, B.M. Steenari, I. Panas, Early hydration and setting of Portland cement  
650 monitored by IR, SEM and Vicat techniques, *Cem. Concr. Res.* 39 (5) (2009) 433–439.

651 [37] G.L. Golewsgi. Improvement of fracture toughness of green concrete as a result of addition of  
652 coal fly ash. Characterization of fly ash microstructure, *Mater. Charact.* 134 (2017) 335–346.

653 [38] N.B. Winter, ‘Scanning Electron Microscopy of Cement and Concrete’, WHD Microanalysis,  
654 Woodbridge, Suffolk, 2012.

655 [39] C. Famy, A.R. Brough, H.F.W. Taylor, The CSH gel of Portland cement mortars: Part I. The  
656 interpretation of energy-dispersive X-ray microanalyses from scanning electron microscopy, with



657 some observations on CSH, AFm and AFt phase compositions, *Cem. Concr. Res.* 33 (9) (2003) 1389–  
658 1398.

659 [40] H.P. Schwan, G. Schwarz, J. Maczuk, H. Pauly, On the low-frequency dielectric dispersion of  
660 colloidal particles in electrolyte solution, *J. Phys. Chem.* 66 (12) (1962) 2626–2635.

661 [41] G. Schwarz, G., A theory of the low-frequency dielectric dispersion of colloidal particles in  
662 electrolyte solution, *J. Phys. Chem.* 66 (12) (1962) 2636–2642.

663 [42] J.B. Hasted, *Aqueous Dielectrics*, Chapman and Hall, London, 1973.

664 [43] A. Serghei, M. Tress, J.R. Sangoro, F. Kremer, Electrode polarization and charge transport at  
665 solid interfaces, *Phys. Rev. B* 80 (18) (2009), 184301.

666 [44] P.B. Ishai, M.S. Talary, A. Caduff, E. Levy, Y. Feldman, Electrode polarization in dielectric  
667 measurements: a Review, *Meas. Sci. Tech.* 24 (10) (2013) 102001 1–21.

668 [45] W.J. McCarter, H.M. Taha, B. Suryanto, G. Starrs, Two-point concrete resistivity measurements:  
669 interfacial phenomena at the electrode–concrete contact zone, *Meas. Sci. Technol.* 26 (8) (2015)  
670 085007 1–13.

671 [46] B. Lothenbach, F. Winnefeld. Thermodynamic modelling of the hydration of Portland cement,  
672 *Cem. Concr. Res.* 36 (2) (2006) 209–226.

673 [47] Y. Elakneswaran, T. Ishida, Development and verification of an integrated physicochemical and  
674 geochemical modelling framework for performance assessment of cement-based materials, *J. Adv.*  
675 *Concr. Technol.* 12 (2014) 111–126.

676 [48] W.J. McCarter, Effects of temperature on conduction and polarization in Portland cement mortar,  
677 *J. Am. Ceram. Soc.* 78 (2) (1995) 411–415.

678

679

680

681

682

683

684

685 **Figure captions**

686

687 **Fig. 1.** (a) Schematic of the Quantomix capsule; (b) close-up of the top windows numbered according  
688 to their position, with the prefix representing the row number and the suffix representing the column  
689 number; (c) test cell for electrical measurements; and (d) layout of tile numbered according to the  
690 sequence of image collection, overlain on the windows shown in (b).

691

692 **Fig. 2.** Stitched BSE images showing the progress of cement hydration on all windows: (a) 30-min;  
693 (b) 4.5-h; (c) 12-h and (d) 18-h after gauging.

694

695 **Fig. 3.** Time-lapse imaging of Window 14 (3-6 on Fig. 1(b)) with images taken every ~35-min over  
696 the initial 24-h after gauging. Images are arranged from left-to-right and top-to-bottom in the order of  
697 measurement sequence, with each row displaying successive changes over a ~3-hour period. Each  
698 window is 300 $\mu$ m square.

699

700 **Fig. 4.** Enlarged BSE images of the progressive formation of Portlandite crystals indicated by the  
701 rectangles in Fig. 3 at (a) ~4-h (image 8), (b) ~8-h (image 14), (c) ~12-h (image 21) and (d) ~18-h  
702 (image 32). (e) and (f) are enlarged images of areas indicated by the circles on image 14 in Fig. 3  
703 where the first indication of a reduction in water-content is evident.

704

705 **Fig. 5.** Selected time-lapse images of Window 2 (1-4 on Fig. 1(b)) at (a) the initial state, (b) 6-h, (c) 8-  
706 h, (d) 10-h, (e) 12-h and (f) 24-h after gauging. The bright dots at the initial state are the upper part of  
707 the cement particles while the dark areas represent the interstitial aqueous phase. A porous surface is  
708 evident as the water-level has reduced, revealing partially hydrated cement grains which are bright  
709 and capillary pores which are much darker.

710 **Fig. 6.** Enlarged images of selected areas of Window 2 (indicated on Fig. 5(f)) taken at 24 hours after  
711 gauging showing the presence of: (a) and (b) large Portlandite crystal surrounded by cement grains

712 covered by fibrillar outgrowths comprising C-S-H and some longer needle-like (ettringite) crystals;  
713 (c) and (d) smaller hydration products where the Portlandite crystal is absent.

714

715 **Fig. 7.** Time-lapse images of Fig. 6(d) at (a) 2.5-h; (b) 4-h; (c) 6.5-h; (d) 8-h; (e) 10-h; and (f) 12.5-h  
716 after gauging.

717

718 **Fig. 8.** Observed time of the first appearance of Portlandite crystals and the first indication of a  
719 reduction in water-content resulting from hydration reactions. The mean values are indicated in the  
720 Figure by the dashed lines.

721

722 **Fig. 9.** (a) BSE images of Windows 11, 12, 17, 18, 24 and 25 (see Fig. 1(d)) after 24-h hydration; (b)  
723 respective EDX maps of Windows after 24-h hydration where red represents potassium, green is  
724 sulphur, yellow is calcium, pink is silicon and cyan represents areas rich in aluminum; (c) is enlarged  
725 image of rectangle indicated on Window 18 in (a) with the respective EDX map shown in (d); green  
726 represents areas rich in aluminum, yellow is calcium and cyan is silicon; and (e) is typical elemental  
727 composition of selected areas in (d). These figures appear in colour in the electronic version.

728

729 **Fig. 10.** Schematic showing (a) double layer polarization and (b) interfacial polarization.

730

731 **Fig. 11.** (a) Conductivity,  $\sigma$ , and its derivative,  $d\sigma/dt$ , during initial 24hours, with Regions I–VI  
732 indicated; (b) normalized relative permittivity,  $\epsilon_r$ , at five selected spot frequencies; and (c) variation  
733 in internal temperature of cement paste.

734

735

736

737

738

739

740 **Video Captions**

741 **Video 1.** Animation of Window 14 (3-6 on Fig. 1(b)) displaying Portlandite formation and general  
742 microstructural densification over the 24-h test period.

743

744 **Video 2.** Animation of Portlandite growth in Window 14 over the 24-h test period.

745

746 **Video 3.** Animation of Window 2 (1-4 on Fig. 1(b)) where fewer numbers of Portlandite precipitates  
747 are evident over the 24-h test period.

748

749 **Video 4.** Animation of precipitates on grain surfaces within the area indicated by the rectangle in Fig.  
750 5(f) over the 24-h test period.

751

752

753

754

755

756

757

758

759

760

761

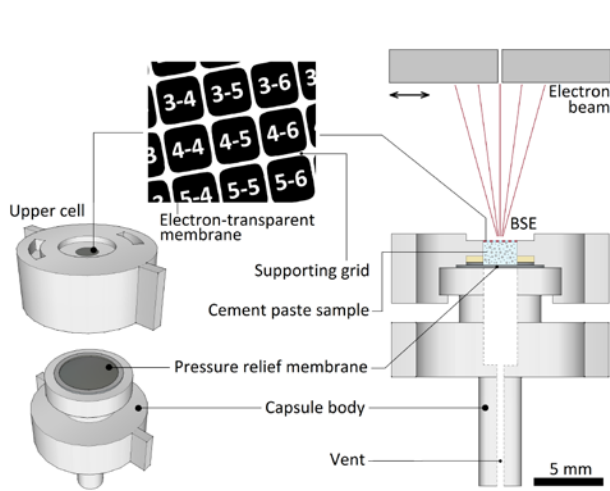
762

763

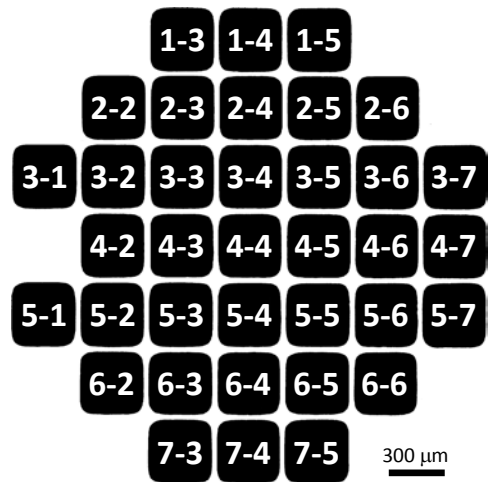
764

765

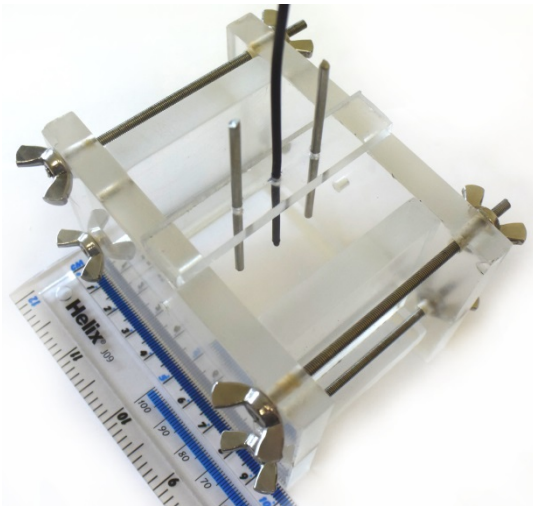
766



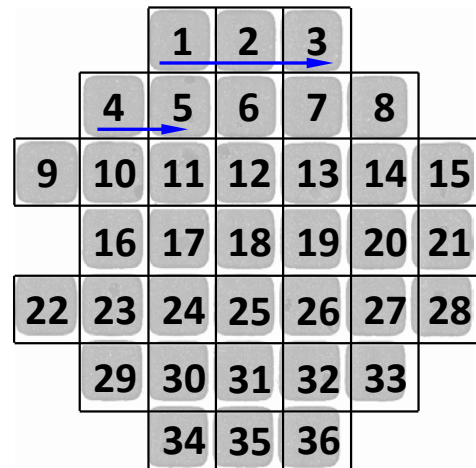
(a)



(b)



(c)



(d)

767  
768  
769

770  
771  
772

773 **Fig. 1.** (a) Schematic of the Quantomix capsule; (b) close-up of the top windows numbered according  
774 to their position, with the prefix representing the row number and the suffix representing the  
775 column number; (c) test cell for electrical measurements; and (d) layout of tile numbered according  
776 to the sequence of image collection, overlain on the windows shown in (b).

777  
778  
779

780  
781  
782  
783  
784  
785  
786  
787  
788  
789  
790  
791  
792  
793  
794  
795  
796  
797  
798  
799  
800  
801  
802  
803  
804  
805  
806  
807  
808

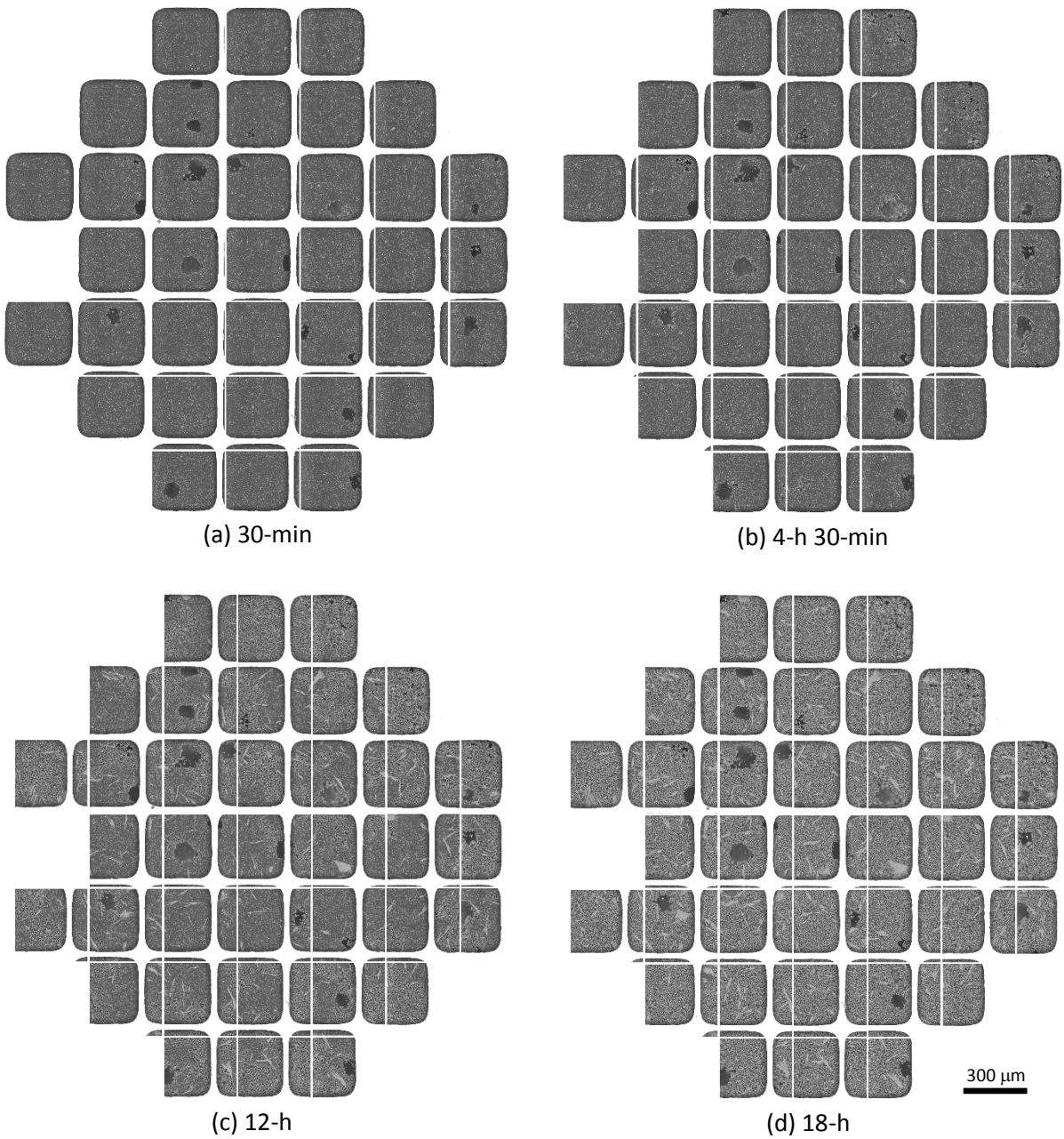
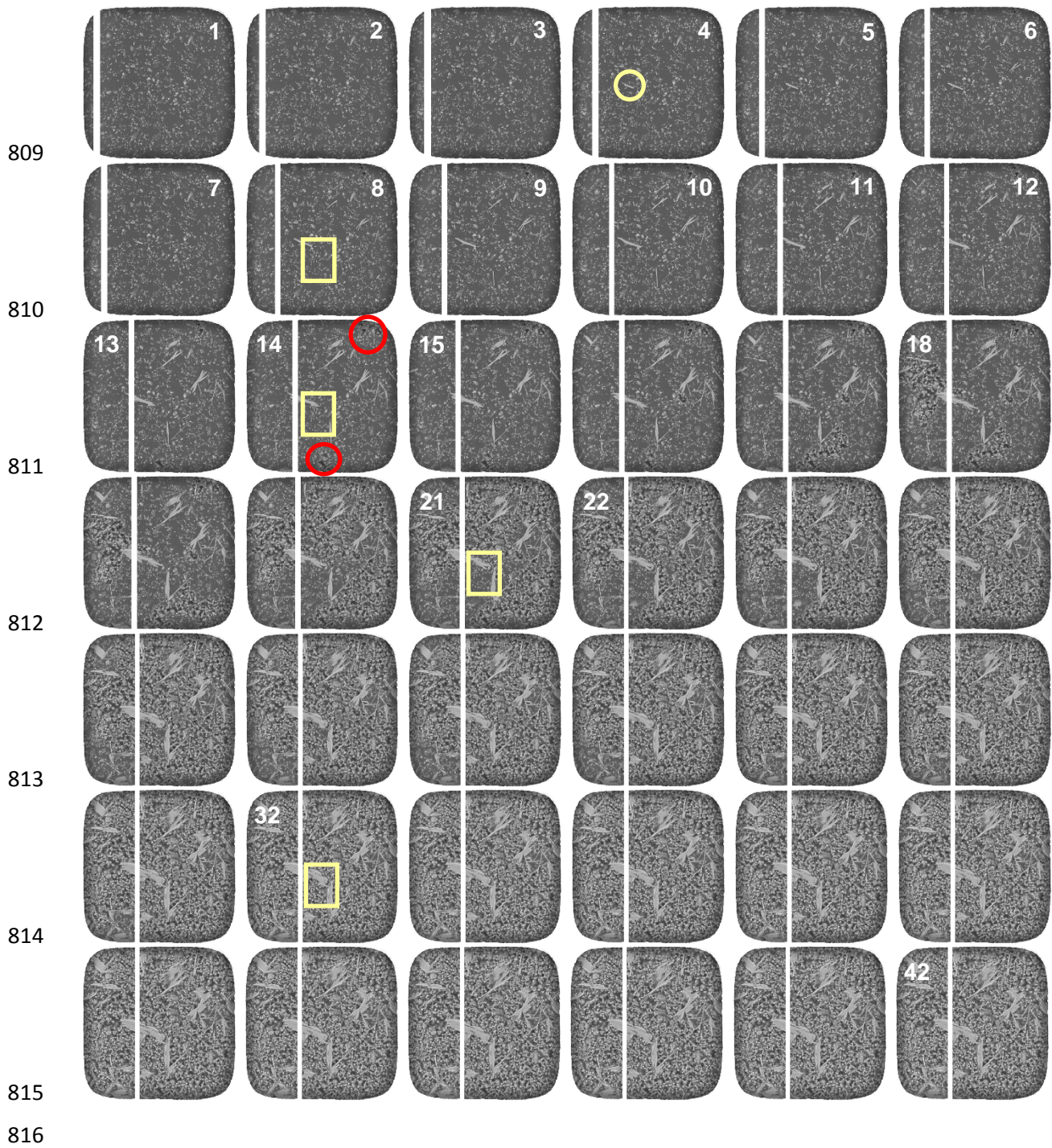


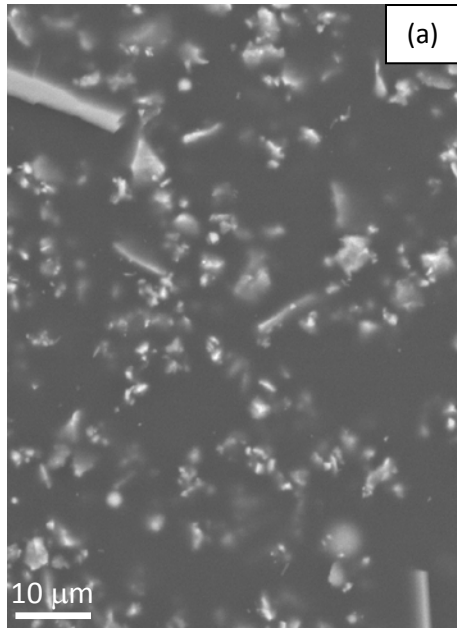
**Fig. 2.** Stitched BSE images showing the progress of cement hydration on all windows: (a) 30-min; (b) 4.5-h; (c) 12-h and (d) 18-h after gauging.



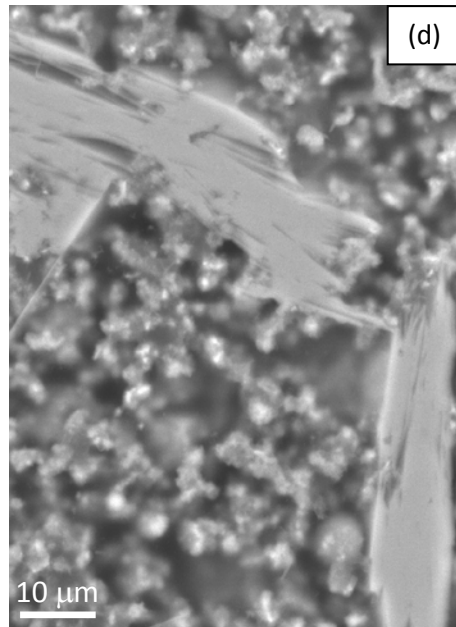
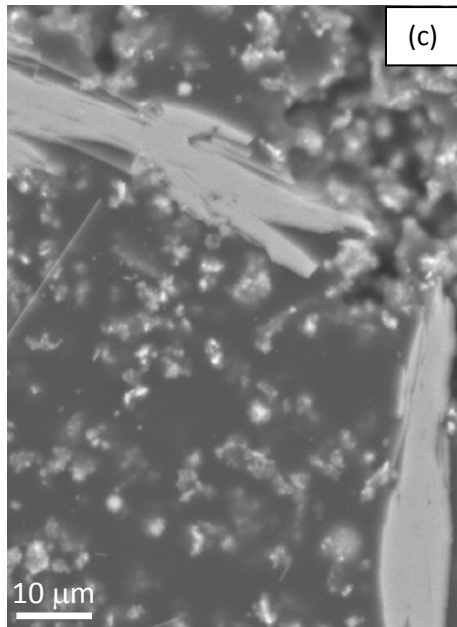
817 **Fig. 3.** Time-lapse imaging of Window 14 (3-6 on Fig. 1(b)) with images taken every ~35-min over the  
 818 initial 24-h after gauging. Images are arranged from left-to-right and top-to-bottom in the order of  
 819 measurement sequence, with each row displaying successive changes over a ~3-hour period. Each  
 820 window is 300 $\mu$ m square.

821  
 822

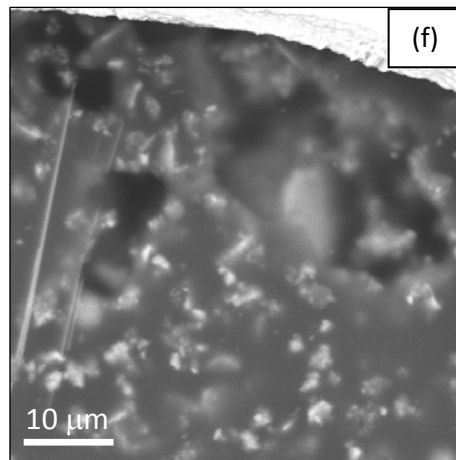
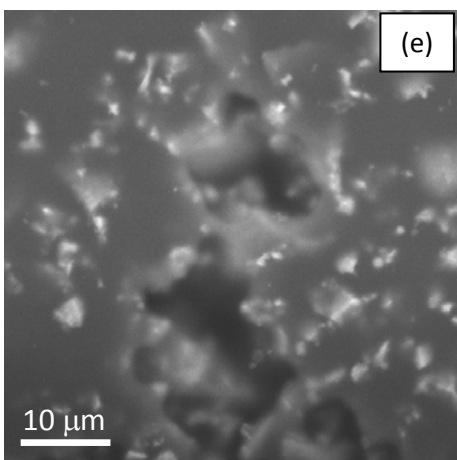
823



824



825





826 **Fig. 4.** Enlarged BSE images of the progressive formation of Portlandite crystals indicated by the  
827 rectangles in Fig. 3 at (a) ~4-h (image 8), (b) ~8-h (image 14), (c) ~12-h (image 21) and (d) ~18-h  
828 (image 32). (e) and (f) are enlarged images of areas indicated by the circles on image 14 in Fig. 3  
829 where the first indication of a reduction in water-content is evident.

830

831

832

833

834

835

836

837

838

839

840

841

842

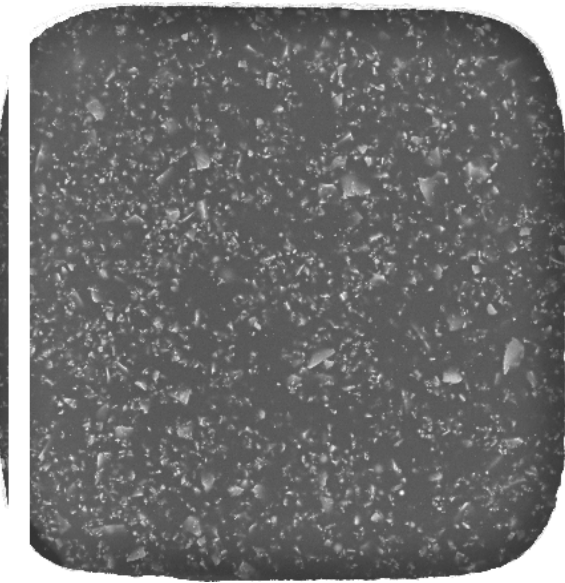
843

844

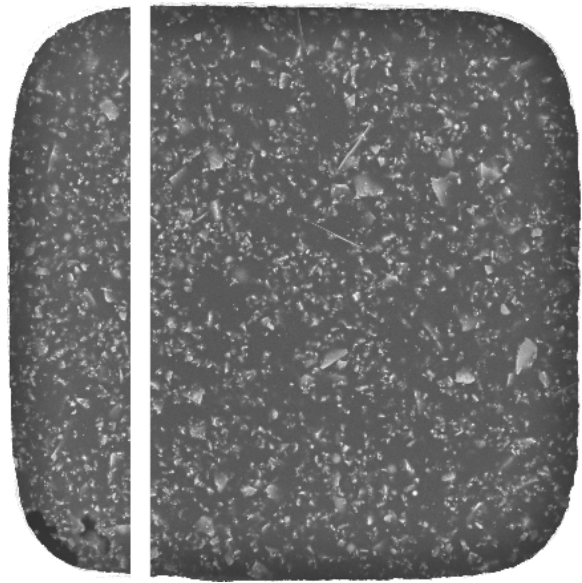
845

846

847  
848

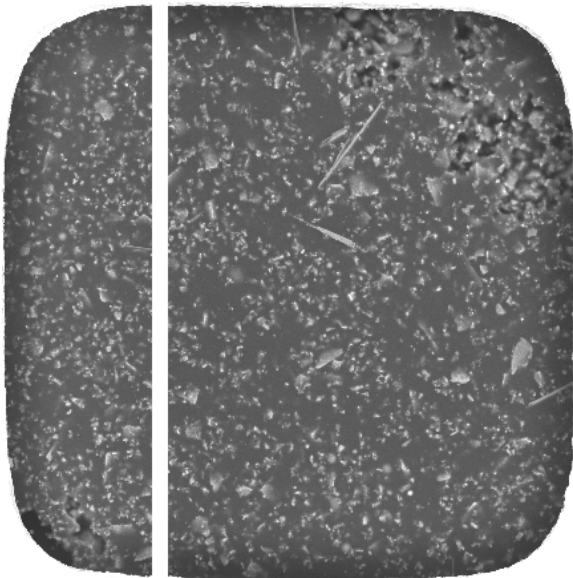


(a) Initial

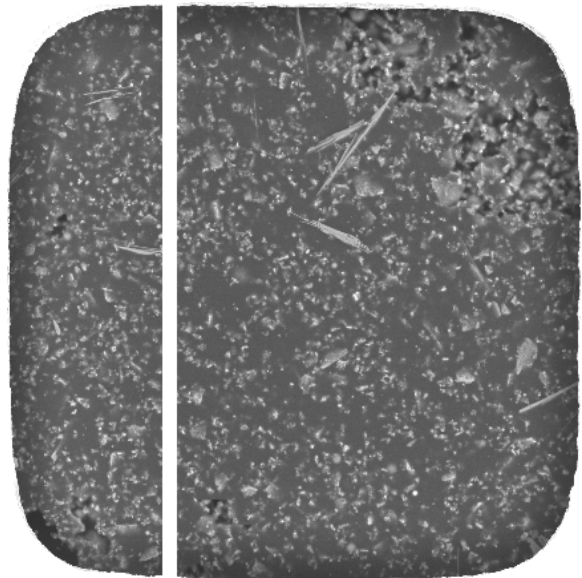


(b) 6-h

849  
850



(c) 8-h

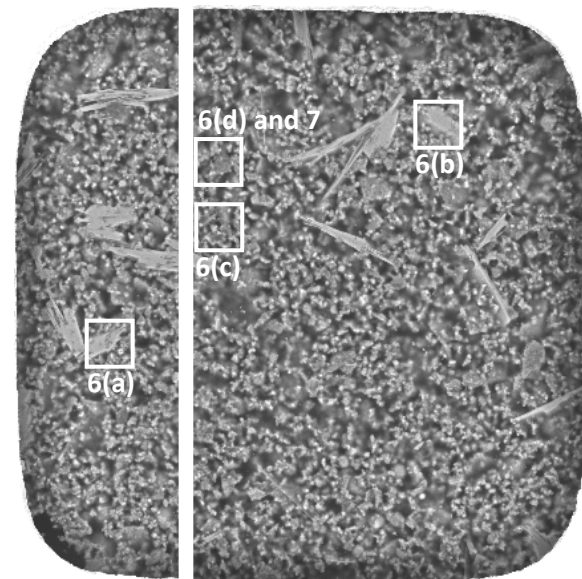


(d) 10-h

851



(e) 12-h



(f) 24-h

50 μm

852 **Fig. 5.** Selected time-lapse images of Window 2 (1-4 on Fig. 1(b)) at (a) the initial state, (b) 6-h, (c) 8-  
853 h, (d) 10-h, (e) 12-h and (f) 24-h after gauging. The bright dots at the initial state are the upper part  
854 of the cement particles while the dark areas represent the interstitial aqueous phase. A porous  
855 surface is evident as the water-level has reduced, revealing partially hydrated cement grains which  
856 are bright and capillary pores which are much darker.

857

858

859

860

861

862

863

864

865

866

867

868

869

870

871

872

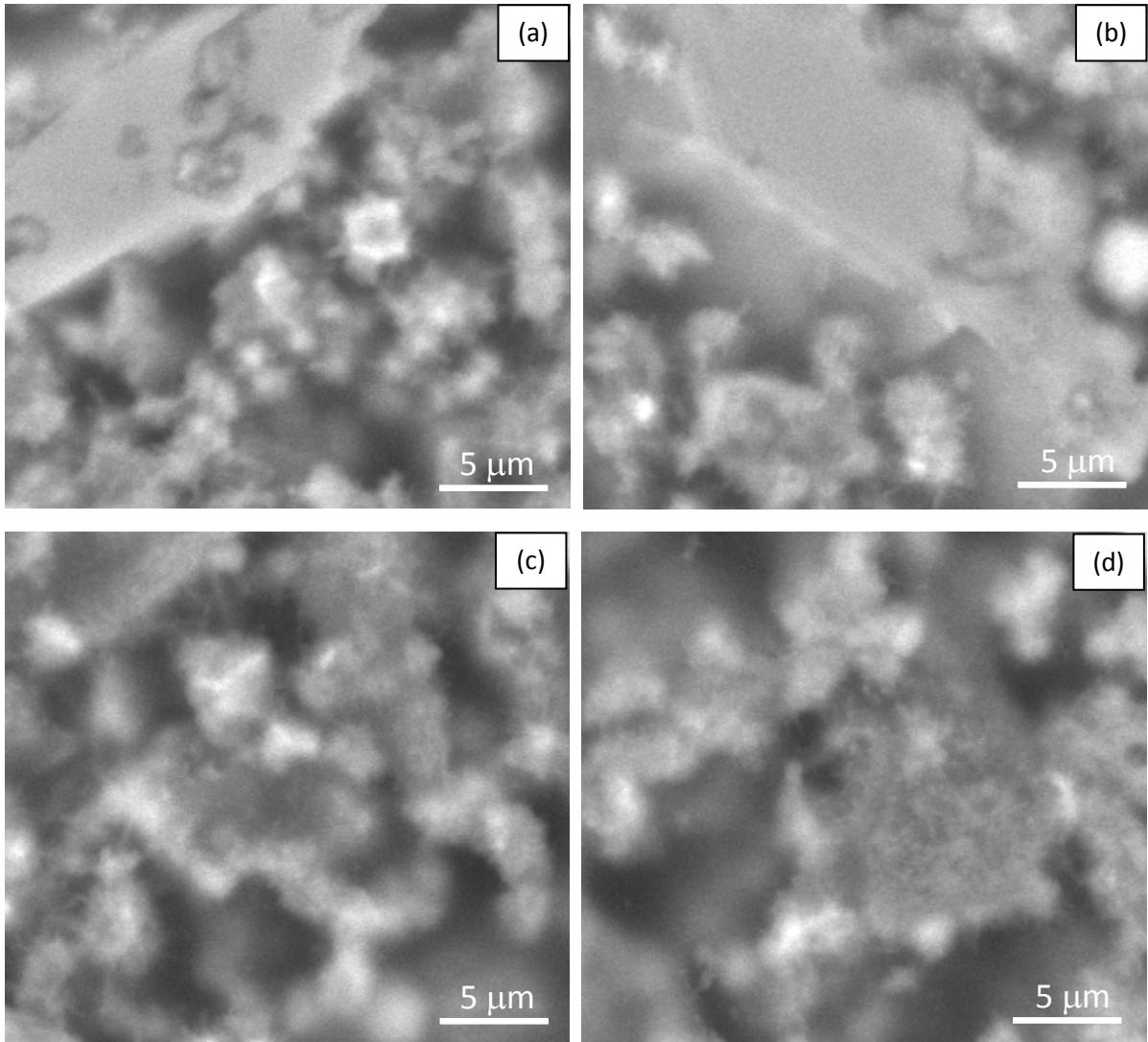
873

874

875

876

877



878

879

880

881 **Fig. 6.** Enlarged images of selected areas of Window 2 (indicated on Fig. 5(f)) taken at 24 hours after  
882 gauging showing the presence of: (a) and (b) large Portlandite crystal surrounded by cement grains  
883 covered by fibrillar outgrowths comprising C-S-H and some longer needle-like (ettringite) crystals; (c)  
884 and (d) smaller hydration products where the Portlandite crystal is absent.

885

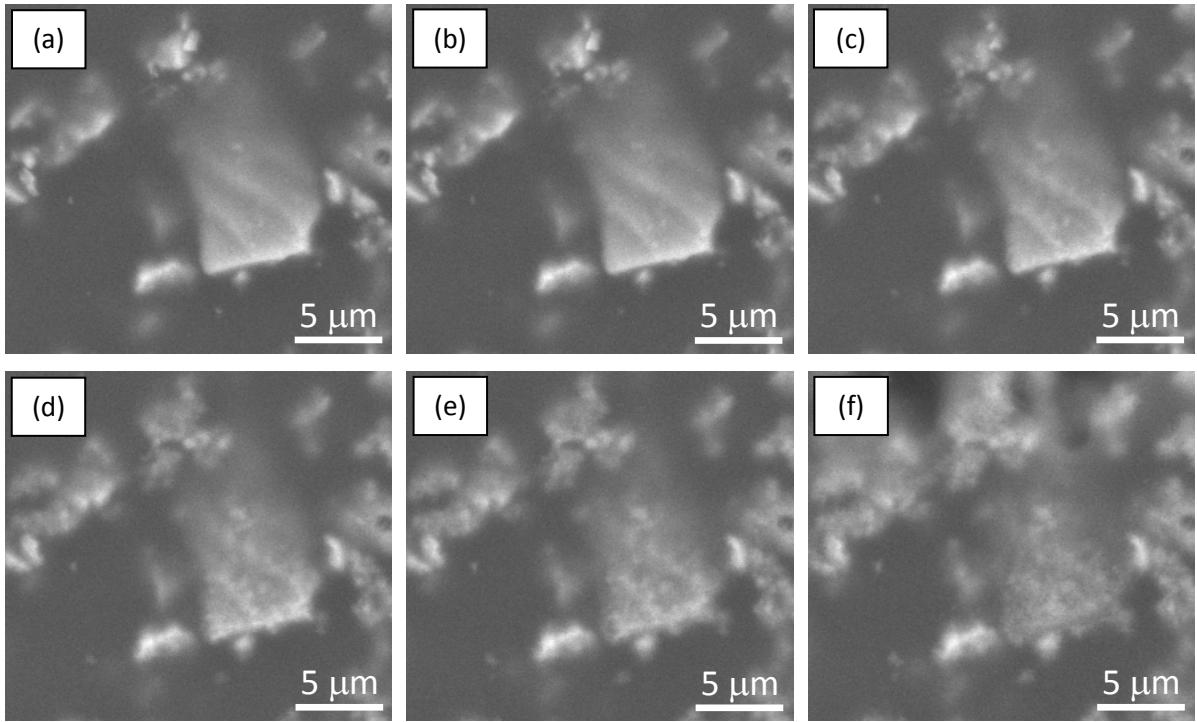
886

887

888

889

890



891

892

893 **Fig. 7.** Time-lapse images of Fig. 6(d) at (a) 2.5-h; (b) 4-h; (c) 6.5-h; (d) 8-h; (e) 10-h; and (f) 12.5-h  
894 after gauging.

895

896

897

898

899

900

901

902

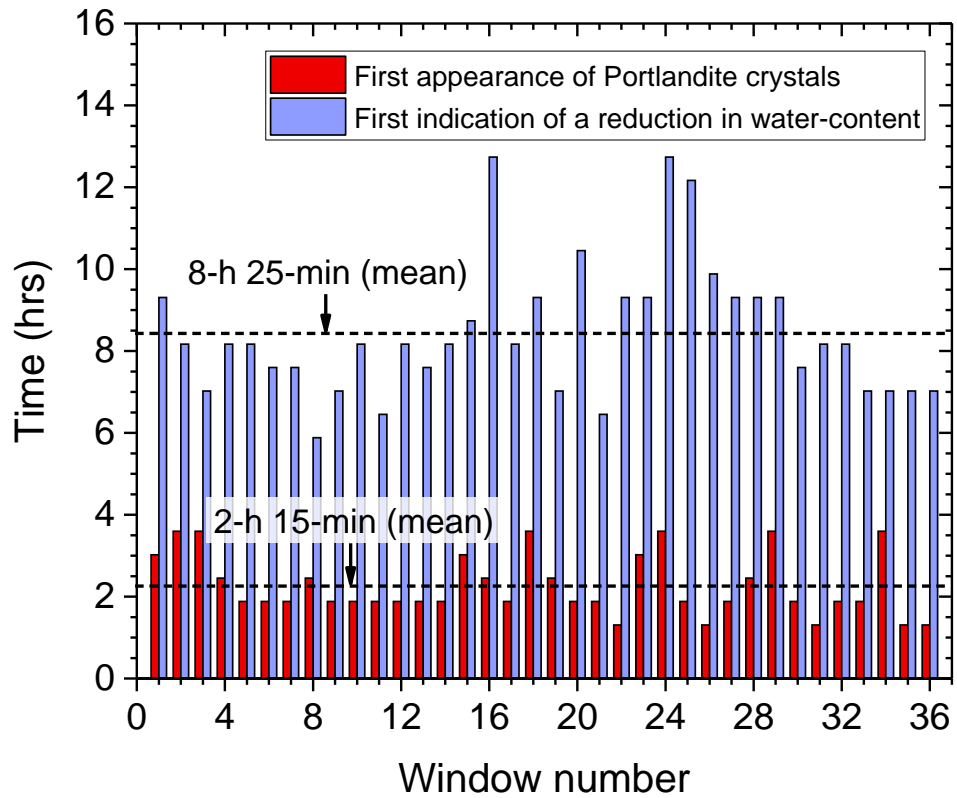
903

904

905

906

907



909

910 **Fig. 8.** Observed time of the first appearance of Portlandite crystals and the first indication of a  
 911 reduction in water-content resulting from hydration reactions. The mean values are indicated in the  
 912 Figure by the dashed lines.

913

914

915

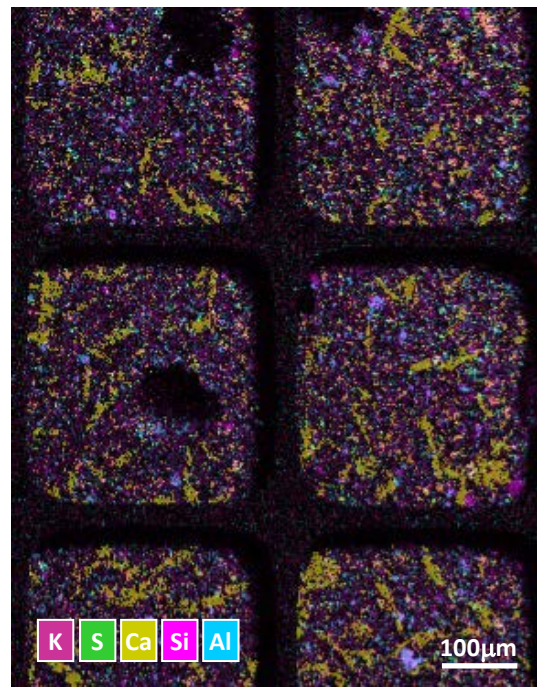
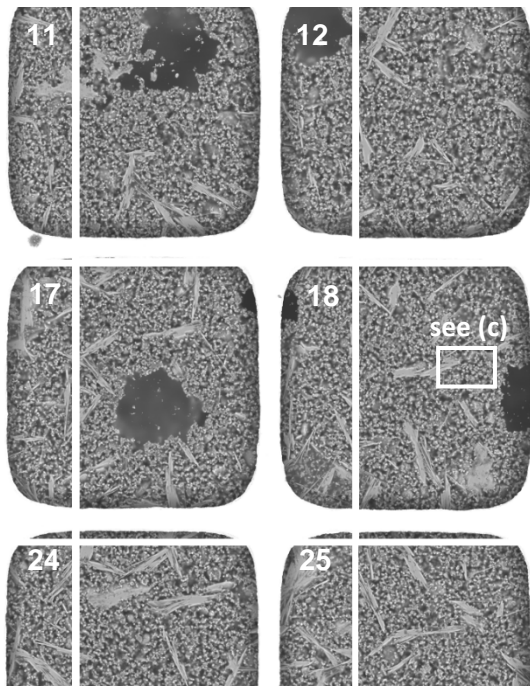
916

917

918

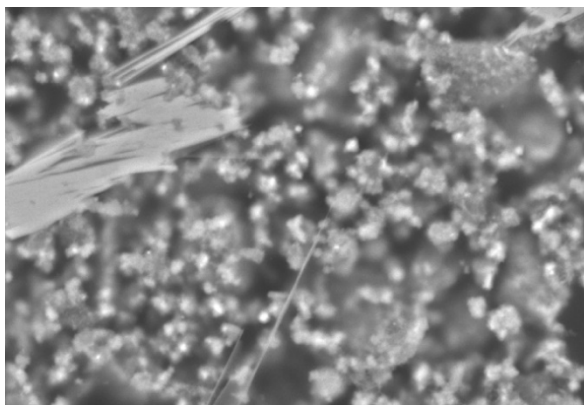
919

920

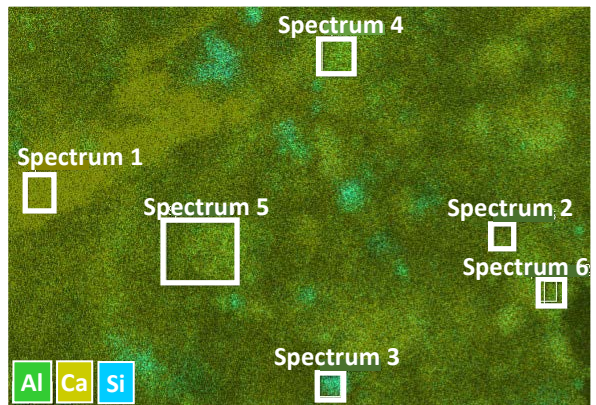


(a)

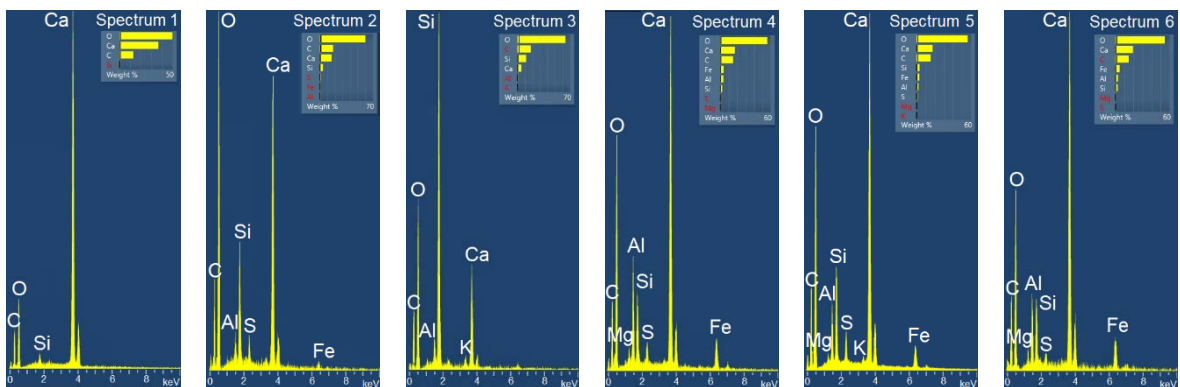
(b)



(c)



(d)



(e)

**Fig. 9.** (a) BSE images of Windows 11, 12, 17, 18, 24 and 25 (see Fig. 1(d)) after 24-h hydration; (b) respective EDX maps of Windows after 24-h hydration where red represents potassium, green is

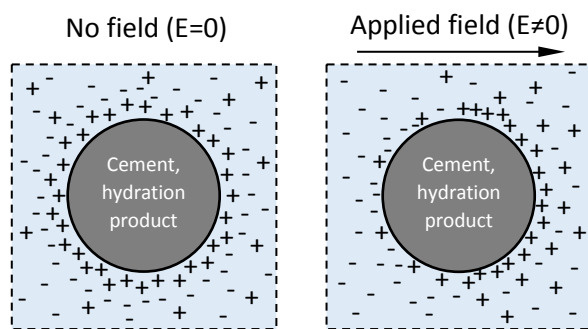
935 sulphur, yellow is calcium, pink is silicon and cyan represents areas rich in aluminum; (c) is enlarged  
936 image of rectangle indicated on Window 18 in (a) with the respective EDX map shown in (d); green  
937 represents areas rich in aluminum, yellow is calcium and cyan is silicon; and (e) is typical elemental  
938 composition of selected areas in (d). These figures appear in colour in the electronic version.

939

940

941

942



943

944

945

946

947

948

(a)

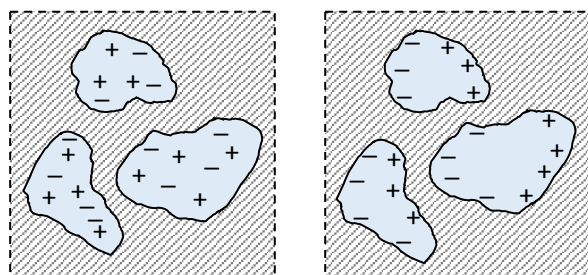
949

950

951

952

953



954

955 **Fig. 10.** Schematic showing (a) double layer polarization and (b) interfacial polarization.

956

957

958

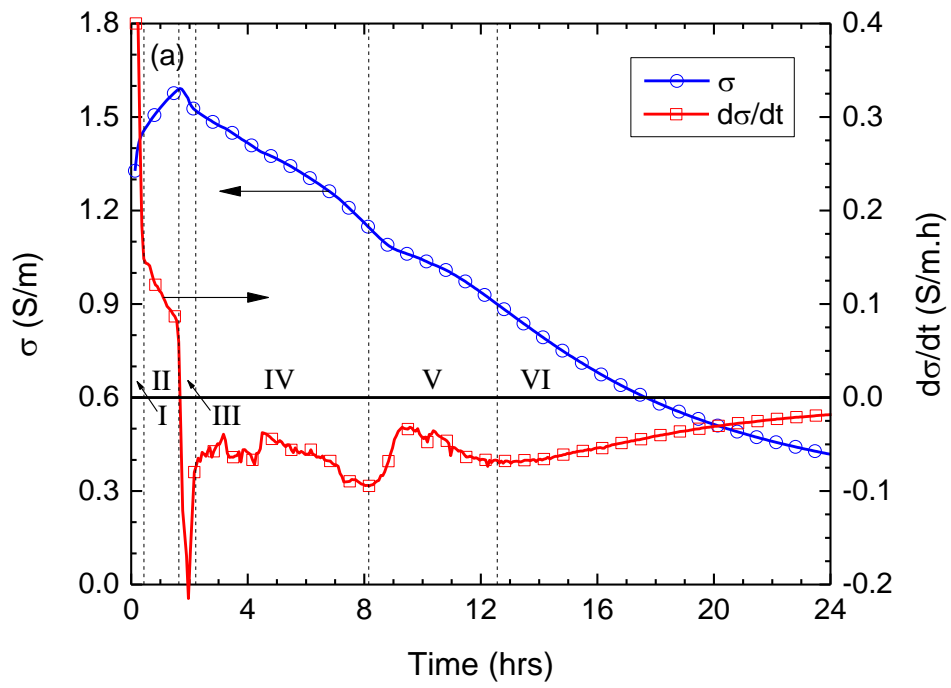
959

960

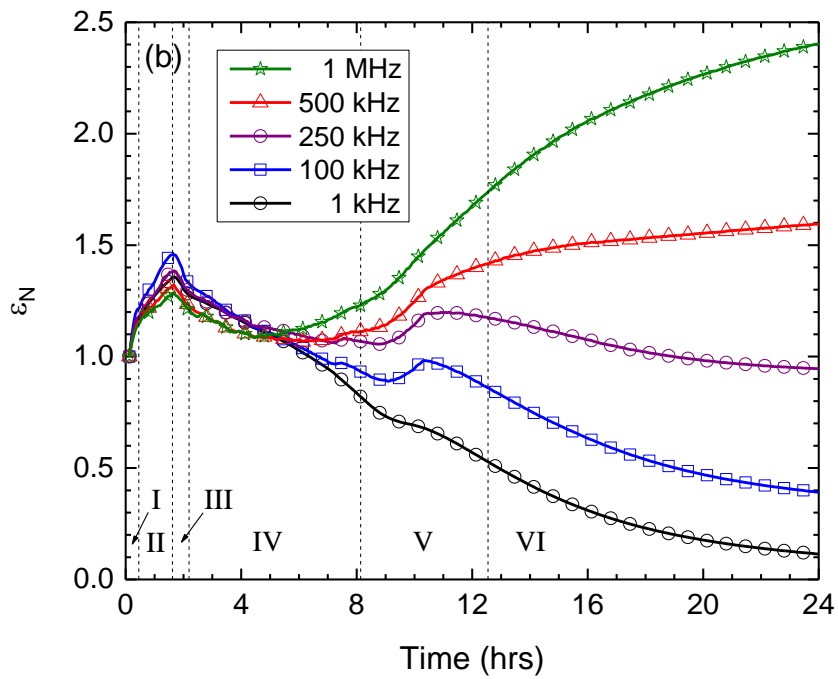
961



962



963

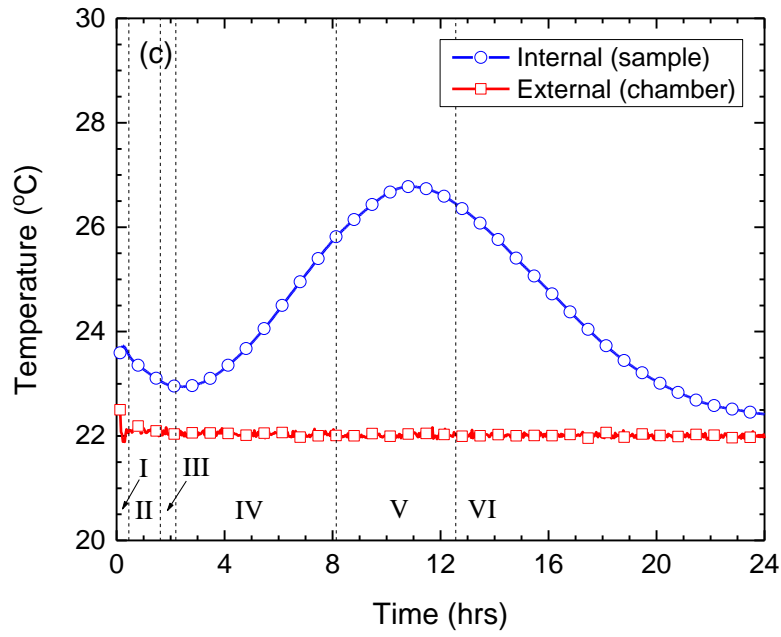


964

965

966

967



968

969 **Fig. 11.** (a) Conductivity,  $\sigma$ , and its derivative,  $d\sigma/dt$ , during initial 24-hours, with Regions I–VI  
 970 indicated; (b) normalized relative permittivity,  $\epsilon_N$ , at five selected spot frequencies; and (c) variation  
 971 in internal temperature of cement paste.

972

973

974

975

976

977

978

979

980

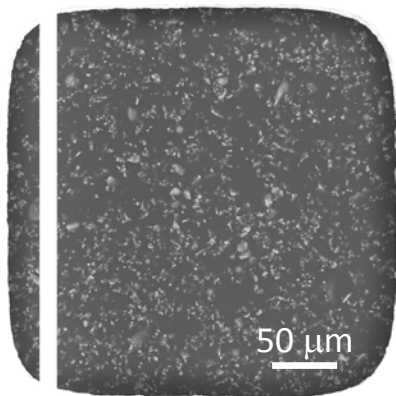
981

982

983

984 **Video thumbnails**

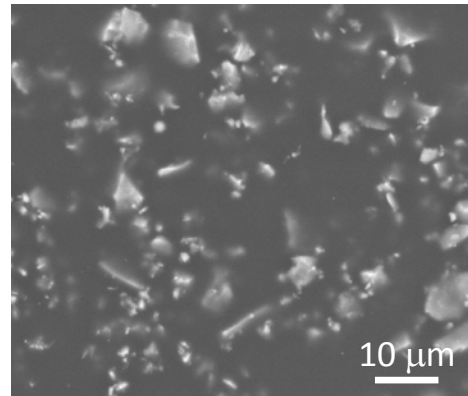
985



986

Thumbnail image for **Video 1**

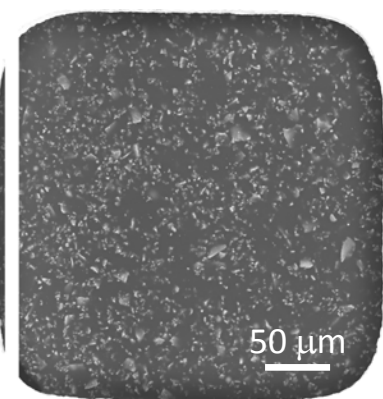
987



Thumbnail image for **Video 2**

988

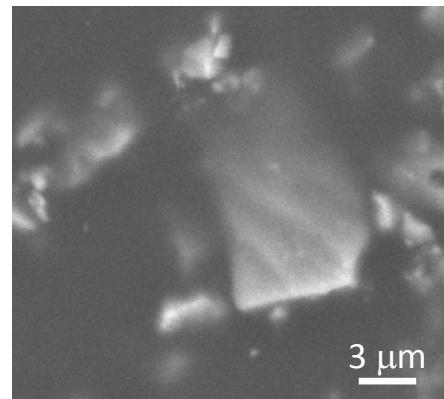
989



990

Thumbnail image for **Video 3**

991



Thumbnail image for **Video 4**

992

993

994

995

996

997

998

999 **Table captions**

1000 **Table 1.** Typical oxide analysis of the cement.

1001 **Table 2.** Initial values of relative permittivity,  $\epsilon_{r,o}(\omega)$ , at selected five spot frequencies.

1002

1003

1004

1005

1006

1007

1008

1009

1010

1011

1012

1013

1014

1015

1016

1017

1018

1019

**Table 1.** Typical oxide analysis of the cement.

Content	By weight (%)
SiO <sub>2</sub>	20.95
Al <sub>2</sub> O <sub>3</sub>	5.20
Fe <sub>2</sub> O <sub>3</sub>	3.42
CaO	59.86
MgO	2.25
K <sub>2</sub> O	0.56
Na <sub>2</sub> O	0.21

1020

1021

**Table 2.** Initial values of relative permittivity,  $\epsilon_{r,o}(\omega)$ , at selected five spot frequencies.

Frequency (kHz)	$\epsilon_{r,o}(\omega)$
1	$7.49 \times 10^6$
100	$2.11 \times 10^3$
250	$5.45 \times 10^2$
500	$2.50 \times 10^2$
1,000 (1 MHz)	$1.42 \times 10^2$

1022